Final report

Shallow crustal heterogeneity in Southern California estimated from earthquake coda waves

Report for SCEC Award #20124
Submitted March 17, 2021

Investigators: Nori Nakata (MIT)

I. Project Overview

A. Abstract

In the box below, describe the project objectives, methodology, and results obtained and their significance. If this work is a continuation of a multi-year SCEC-funded project, please include major research findings for all previous years in the abstract. (Maximum 250 words.)

High-frequency scattered waves contain important information to reveal small-scale structure such as heterogeneities of velocities and attenuation, which should be considered and included for high-frequency ground motion. In this study, we image the 3D small-scale scatterer structure using a rock samples to develop a method, and then apply it to the data in southern California especially in the area around the San Jacinto fault zone, which is still ongoing and for the subject of extension. The small-scale heterogeneities are difficult to image using wavefield migration or waveform inversion, but coda waves contain such information. For example, the peak amplitude time of waveform envelope is delayed when structures along the ray path is highly scattered. We use this phenomenon and apply peak-delay-time tomography at different frequencies to reveal the small-scale heterogeneities using a rock sample to develop the method before we apply it to the San Jacinto fault zone. This laboratory experiment is essential to understand the complex phenomena of scattering. The tomograms show the high heterogeneities are concentrated around the faults, which correspond to the CT scan of the rock sample. Also we numerically calculate the wavefields according to different scattering properties. We will use this tomography method to reveal the scattering properties around the southern California.

B. SCEC Annual Science Highlights

Each year, the Science Planning Committee reviews and summarizes SCEC research accomplishments, and presents the results to the SCEC community and funding agencies. Rank (in order of preference) the sections in which you would like your project results to appear. Choose up to 3 working groups from below and re-order them according to your preference ranking.

Ground Motion Prediction (GMP)
Seismology

C. Exemplary Figure

Select one figure from your project report that best exemplifies the significance of the results. The figure may be used in the SCEC Annual Science Highlights and chosen for the cover of the Annual Meeting Proceedings Volume. In the box below, enter the figure number from the project report, figure caption and figure credits.

Figure 4: Simplified CT image of internal fracture network (left) and spatial distribution of $\Delta log(t_p)$ values for Darley Dale Sandstone. Logarithmic peak delay variations are shown in the lower color bar while diamonds show the PZT positions. Only regions crossed by a minimum of 5 rays are displayed. Azimuthal coverage of model blocks (and so confidence) is reduced towards the edges and outside the region delineated by the receivers. Diamonds indicate receivers used in mapping. The bounding boxes indicate the dimensions of the sample.

D. SCEC Science Priorities

In the box below, please list (in rank order) the SCEC priorities this project has achieved. See *https://www.scec.org/research/priorities* for list of SCEC research priorities. *For example: 6a, 6b, 6c*

4a, 4b, 4d

E. Intellectual Merit

How does the project contribute to the overall intellectual merit of SCEC? *For example: How does the research contribute to advancing knowledge and understanding in the field and, more specifically, SCEC research objectives? To what extent has the activity developed creative and original concepts?*

Small-scale heterogeneities are necessary parameters for high-frequency ground motion prediction, but the estimation of them is not trivial because of the physical limitation of our tomography methods. Therefore we need to rely on stochastic approaches, and here we use envelope peak-delay time. The results of peak-delay-time tomography are encouraging to show the high heterogeneities around the fault zones.

F. Broader Impacts

How does the project contribute to the broader impacts of SCEC as a whole? *For example: How well has the activity promoted or supported teaching, training, and learning at your institution or across SCEC? If your project included a SCEC intern, what was his/her contribution? How has your project broadened the participation of underrepresented groups? To what extent has the project enhanced the infrastructure for research and education (e.g., facilities, instrumentation, networks, and partnerships)? What are some possible benefits of the activity to society?*

Small-scale subsurface information is usually not available for earthquake physics, but the nucleation of earthquakes can be in the very small scale. The estimated heterogeneities can be related to stress state and/or friction in the subsurface structure, and hence our results can be used for earthquake source physics and prediction as well.

G. Project Publications

All publications and presentations of the work funded must be entered in the SCEC Publications database. Log in at *http://www.scec.org/user/login* and select the Publications button to enter the SCEC Pubications System. Please either (a) update a publication record you previously submitted or (b) add new publication record(s) as needed. If you have any problems, please email *web@scec.org* for assistance.

II. Technical Report

Introduction

High-frequency scattered waves contain important information to reveal small-scale structure such as heterogeneities of velocities and attenuation, which should be included for high-frequency ground motion modeling (*Mai et al*., 2010; *Olsen and Takedatsu,* 2015; *Nakata and Beroza*, 2015). Such small-scale heterogeneities are considered as a cause of the nonlinear shallow crust effects. High-frequency earthquake coda waves have been used for studying small-scale heterogeneities of subsurface structures (*Aki* 1969; *Aki and Chouet*, 1975) in addition to the complex source radiation (*Zeng et al*., 1993). *Bydlon and Dunham* (2015) presented the effect of structural and complex rupture process with rough faults for high-frequency ground motions using synthetic tests. Note that because these small-scale heterogeneities are below the resolution limits for velocity estimation using conventional seismic travel-time tomography (*Aki et al*., 1976), we often rely on stochastic approaches to image them.

We study envelope peak delay time at different frequency ranges from many earthquakes in Southern California (especially around the San Jacinto fault; inset in Figure 1) and apply "travel" time tomography for the peak delay time to estimate the spatial distribution of the effects of the delay (Figure 1). In heterogeneous media, the envelope of seismic waves is broadened according to the traveling distance (a.k.a. envelope broadening; *Sato*, 1989; *Sato et al.,* 2012), and we can use this delay time to estimate how heterogeneous the medium is (*Saito et al*., 2002).

Our data (Figure 2) show different peak delay times at different frequencies, and the peak delay time has a rough correlation with the propagation distance. In addition, the correlation is stronger for higher frequencies, which can be explained by the fact that the high-frequency waves are sensitive to small-scale heterogeneities. Essentially, *Takahashi et al.* (2009) use this frequency-dependent envelope peak delay times to estimate the scattering parameters as a function of space. To understand more the scattering phenomena and heterogeneities, we apply a laboratory experiment.

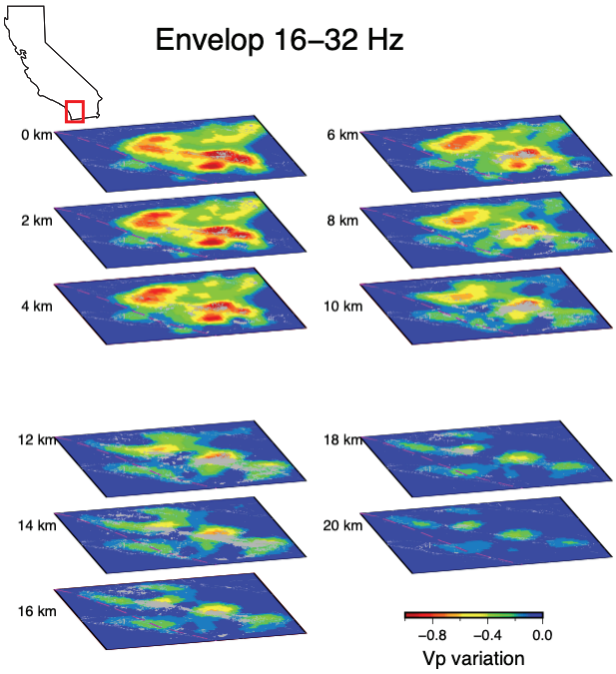

Figure 1. Depth slices of tomograms for envelope peak delay time at 16-32 Hz. The color indicates the velocity difference compared to the direct P-wave travel-time tomography maps in km/s, and red means that the delay of the envelope peak time is large (i.e., envelope broadening is significant and medium is highly heterogeneous) The gray dots show hypocenter location of earthquakes used. The red square of the inset indicates the location of the velocity map, where we have the San Jacinto fault zone.

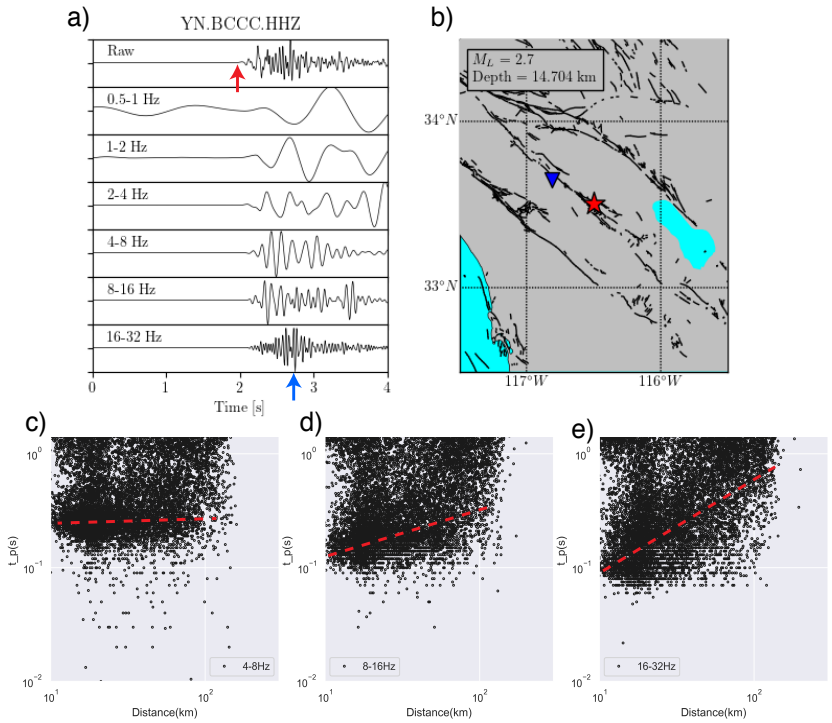

Figure 2. (a) Example of our data of waveforms related to the earthquake (red star) and station (blue triangle) pair shown in panel (b). The red and blue arrows indicate the arrival time of direct wave and the peak delay time of the envelope. (c-e) Distribution of peak delay time (vertical axis) and the propagation distance (i.e., offset of earthquakes and receivers) for all earthquake-station pairs. The red dashed lines show the linear-regression approximation of the distribution.

Laboratory experiment

We developed a tomography method for physical parameter estimation using coda-wave peaks. Two attached documents are the manuscripts to be submitted soon. Peak-delay time tomography can reveal the scattering properties and be sensitive to the faults, and we develop a workflow of this tomography using the laboratory data. However, we understand that it is not very stable and we have to have parameter tuning obtain reasonable results. Eventually, as shown in the attachments, we developed a theory, validated using numerical tests, and then applied it to laboratory data. This method is useful for crustal scale data in California.

References

Aki, K. (1969) Analysis of the seismic coda of local earthquakes as scattered waves, *J. Geophys. Res.*, **74**(2), 615-631.

Aki, K. and B. Chouet (1975) Origin of coda waves: Source, attenuation, and scattering effects, *J. Geophys. Res.,* **70**(23), 3322-3342.

Aki, K., A. Christoffersson, and E. S. Husebye (1976) Three-dimensional seismic structurre of the lithosphere under Montana LASA, *Bull. Seism. Soc. Am.*, **66**(2), 501-524.

Benson, P. M., Thompson, B. D., Meredith, P. G., Vinciguerra, S., & Young, R. P. (2007). Imaging slow failure in triaxially deformed Etna basalt using 3D acoustic-emission location and X-ray computed tomography. *Geophysical Research Letters*, *34*(3). *https://doi.org/10.1029/2006gl028721*

Cionoiu, S., Moulas, E., & Tajčmanová, L. (2019). impact of interseismic deformation on phase transformations and rock properties in subduction zones. *Scientific Reports*, *9*(1), 1–6.

De Siena, L., Calvet, M., Watson, K. J., Jonkers, A. R. T., & Thomas, C. (2016). Seismic scattering and absorption mapping of debris flows, feeding paths, and tectonic units at Mount St. Helens volcano. *Earth and Planetary Science Letters*, *442*, 21–31. https://doi.org/10.1016/j.epsl.2016.02.026

Heap, M. J., Baud, P., Meredith, P. G., Bell, A. F., & Main, I. G. (2009). Time-dependent brittle creep in Darley Dale sandstone. *Journal of Geophysical Research: Solid Earth*, *114*(B7).

Falls, S. D., Young, R. P., Carlson, S. R., & Chow, T. (1992). Ultrasonic tomography and acoustic emission in hydraulically fractured Lac du Bonnet Grey granite. *Journal of Geophysical Research*, *97*(B5), 6867. https://doi.org/10.1029/92jb00041

Fazio, M. (2017, January). *Dynamic Laboratory Simulations of Fluid-Rock Coupling with Application to Volcano Seismicity and Unrest* (PhD Thesis). University of Portsmouth, School of Earth and Environmental Sciences.

Ji, S., & Wang, Q. (2011). Interfacial friction-induced pressure and implications for the formation and preservation of intergranular coesite in metamorphic rocks. *Journal of Structural Geology*, *33*(2), 107–113.

Mai, P. M. W. Imperatori, and K. B. Olsen (2010) Hybrid broadband ground-motion simulations: Combining long-period deterministic synthetics with high-frequency multiple S-to-S backscattering, *Bull. Seism. Soc. Am.,* **100**(5A), 2124-2142.

Nakata, N. and G. C. Beroza (2015) Stochastic characterization of mesoscale seismic velocity heterogeneity in Long Beach, California, *Geophys. J. Int.,* **203**, 2049-2054.

Olsen, K. B. and R. Takedatsu (2015) The SDSU broadband ground-motion generation module BBtoolbox version 1.5, *Seismol. Res. Lett.*, **86**(1), 81-88.

Renard, F., McBeck, J., Kandula, N., Cordonnier, B., Meakin, P., & Ben-Zion, Y. (2019). Volumetric and shear processes in crystalline rock approaching faulting. *Proceedings of the National Academy of Sciences*, *116*(33), 16234–16239.

Saito, T., H. Sato, and M. Ohtake (2002) Envelope broadening of spherically outgoing waves in three-dimensional random media having power law spectra, *J. Geophys. Res.*, **107**(B5), ESE 3.

Sato, H. (1989) Broadening of seismogram envelopes in the randomly inhomogeneous lithosphere based on the parabolic approximation: Southeastern Honshu, Japan, *J. Geophys. Res.*, **94**(B12), 17735-17747.

Sato, H., M. C. Fehler, and T. Maeda (2012) Seismic wave propagation and scattering in the heterogeneous Earth, 2 edn, Springer.

Stanchits, S., Vinciguerra, S., & Dresen, G. (2006). Ultrasonic Velocities, Acoustic Emission Characteristics and Crack Damage of Basalt and Granite. *Pure and Applied Geophysics*, *163*(5), 975–994. https://doi.org/10.1007/s00024-006-0059-5

Takahashi, T., H. Sato, T. Nishimura, and K. Obara (2009) Tomographic inversion of the peak delay times to reveal random velocity fluctuations in the lithosphere: method and application to northeastern Japan, *Geophys. J. Int.*, **178**, 1437-1455.

Thompson, B. D., Young, R. P., & Lockner, D. A. (2009). Premonitory acoustic emissions and stick-slip in natural and smooth-faulted Westerly granite. *Journal of Geophysical Research: Solid Earth*, *114*(B2).

Yoshimitsu, N., Furumura, T., & Maeda, T. (2016). Geometric effect on a laboratory-scale wavefield inferred from a three-dimensional numerical simulation. *Journal of Applied Geophysics*, *132*, 184–192.

Zeng, Y., K. Aki, T.-L. Teng (1993) Mapping of the high-frequency source radiation for the Loma Prieta earthquake, California, *J. Geophys. Res.*, **98**(87), 11981-11993.

Mapping Faults in the Laboratory with Seismic Scattering 1: The Laboratory Perspective

Key Points:

- Acoustic emission micro-tomography identifies zones of intense strain in deforming rock samples.
- Peak delay monitoring identifies fracture nucleation, fault coalescence and sample failure.
- Peak delays map structural heterogeneity and monitor deformation-induced structural changes.

Abstract

Seismic waves produced by stressed and deforming rocks lose coherence when they cross regions of high heterogeneity. The delay in the arrival of maximum seismic energy amplitude (peak delay), an essential attribute to model earthquake source characteristics, is increasingly used to map complex crustal geology, heterogeneous reservoirs, and fault networks. However, no laboratory calibration for the sensitivity of this parameter to fractures is currently available due to both experimental challenges and the difficulty in modelling wavefields in the near field. In this study, peak delays have been measured and mapped in space in the frequency range 50 kHz to 1 MHz using Acoustic Emission (AE) data recorded during a triaxial deformation experiment of Darley Dale Sandstone (DDS). Peak delays can increase dramatically throughout the experiment, but their behaviour depends on frequency and, especially, anomalous azimuth-dependent scattering. The frequency-dependence highlights dependence on strain. At low frequencies, peak delays are sensitive to surface waves generated at the sample boundaries, but they also mark the zones of shadow and intense/intermediate strains expected for an heterogeneous sample. At high frequencies, peak delays detect the zone of intense strain corresponding to the post-deformation shear zone. Temporal variations of peak delays show a frequency-dependent sensitivity to fracture nucleation, fault coalescence and sample failure. Scattering from these heterogeneities produces waves reverberating through seismic coda if the source-station path is close to an acoustic boundary, such as the fault zone or the sample boundaries. Our results confirm that peak delay has notable sensitivity to heterogeneity and can map and monitor structural- and deformation-induced changes in the near-field. The companion modelling paper tests this sensitivity and the corresponding imaging potential.

1 Introduction

When seismic waves propagate into the Earth, they suffer energy losses due to scattering and reverberations on Earth heterogeneities (Sato et al., 2012). Separating the competing effects of seismic anisotropy, heterogeneous scattering, and absorption is a tough challenge at the field scale (Chapman, 2003; Durán et al., 2018; Fehler, 1991), particularly in active fault systems (Bianco et al., 2005; Napolitano et al., 2019; Sketsiou et al., 2020). Seismic scattering is efficient at imaging fluid-filled fracture networks (Carcione & Picotti, 2006; Main et al., 1990); thus, it is increasingly used as a mapping tool for faults (Maercklin et al., 2004; Napolitano et al., 2019). Heterogeneous scattering increases the duration and complexity of ground motion, even when just a few kilometres away from the epicentre (Imperatori & Mai, 2015). In near-source studies, this role has often been disregarded or corrected in an approximate manner (Ripperger et al., 2008), using the principle that the wavelength (λ) is much larger than the propagation distance.

Seismic scattering is a crucial marker of increased Earth heterogeneity in the far field, i.e., when the propagation distance is much larger than λ. Takahashi et al. (2007, 2009) and Tripathi et al. (2010) developed a tomographic method using the Markov approximation (Saito, 2002) to map crustal heterogeneity. The imaging attribute is the time delay between the onset of the wave and the maximum amplitude of the seismic energy (the *peak delay*). The authors observed spatial correlations of high peak delays with the location of quaternary age volcanoes. Expanding further on the technique, Calvet et al. (2013) and Borleanu et al. (2017) used high peak delays to mark deformation in the Pyrenees and tectonic processes in Romania, respectively. More recently, Napolitano et al. (2019) demonstrated that peak delays, in conjunction with coda attenuation mapping, can reconstruct the complex space-frequency evolution of seismically active fluid-filled fault systems, tracking shorter-scale cross faulting

with increasing frequencies. Maps of high peak delays agree well with physical attributes such as fracture patterns that block the lateral migration of fluids across the network This study suggests a potential of frequency-dependent peak delay for imaging and monitoring fracturing- and deformation-related processes using frequency-dependent peak delays.

Any mapping and monitoring attribute requires well-constrained laboratory calibration to be considered reliable. Data from laboratory experiments suggest that amplitude-dependent attributes, particularly seismic attenuation, can better characterize rock-physics attributes like pore space (Di Martino et al., 2021) and fluid type (Adam et al., 2009) when paired with seismic phase data. Some experiments have reproduced specific conditions observed in the field to calibrate the ability of attenuation parameters to image fault structures (Barnhoorn et al., 2018; Tisato & Quintal, 2014). Often used are Acoustic Emissions (AE), the laboratory analogue to earthquake data, as they provide a window into the near-field scattering regime (Zhang et al., 2019).

Rock-physics experiments are already a powerful tool for reproducing deformation and fracturing in porous media under stress conditions that are known and controlled (Harnett et al., 2018). As the density of fractures increases, AE waveform data becomes highly sensitive to deformation structure with significant variations in P- and S-wave velocities (e.g., Schubnel et al., 2003). In contrast, active surveys conducted using synthetic media have demonstrated a geometrical bias to scattering parameters due to the relative positioning of heterogeneous structures and the AE acquisition array (Rao & Wang, 2009). Numerical studies identify a dependence of scattering attenuation parameters on frequency, where the inverse quality factor, mapping attenuation, is linearly dependent on fracture density (Fang et al., 2013; Vlastos et al., 2007). Furthermore, within the late coda of simulated AE, Yoshimitsu et al. (2016) identified low-frequency, high-amplitude arrivals in cylindrical steel samples. The authors attributed these to surface waves acting after the AE energy interacted with the sample boundaries.

Shear zones and competent layers represent viscosity heterogeneities within a rock mass. In addition to the initial heterogeneity (grain size, mineralogy, porosity, initial crack damage) at the onset of the loading, a rock sample suffers increasing crack damage and stress concentrations. A heterogeneously deformed sample can be divided into three zones: strain-forbidden zone, intensive strain zone, and intrusion zone, having precise distributions relative to the pistons and direction of normal stress (Ji and Wang, 2011). In the field, peak delays are sensitive to heterogeneity. In controlled experiments, the expected distribution of heterogeneity is known, and can be used to calibrate the frequency-dependent sensitivity of peak delays.

This study examines the spatial and temporal variation of peak delays measured from AE in a sample of Darley Dale Sandstone (DDS) as an analogue for crustal-scale interfaces observed in the near field and for a high scattering regime. The mechanical behaviour of DDS under conventional triaxial conditions is well reported in the literature (Baud & Meredith, 1997; Heap et al., 2009; King et al., 2021). We conducted several focused experiments to relate the onset and development of cracking to the different deformation stages (i.e., compaction, dilatancy and shear) by analysing the AE recorded by an array of piezoelectric transducers (PZT) as the fault zone structure develops.

This sample set and the generated AE dataset have been previously analysed for waveform picking and fracturing source mechanisms (King et al., 2020, 2021). Using their data, we focus on frequency and time dependencies of peak delays as a quantity sensitive to medium heterogeneity. Results are analysed and related to a developing fracture network and strain distribution to provide quantitative support for mapping and monitoring faults with the attribute and better understanding the physics underlying their changes. Specifically, we present new methods to:

i. pick “Beyond the Direct Wave” (BYD) onsets following a time-frequency transformation of the signal (Constant-Q Transform, CQT);

ii. calculate the average waveform and dominant frequency content and define the peak delay as the time difference between the BYD onset and the maximum amplitude arrival of energy in the ultrasonic coda;

iii. assess the time-dependent coda variations in frequency and amplitude;

iv. produce peak delay maps for arrivals to individual stations.

We finally discuss the potential of these attributes for monitoring in the field, with particular emphasis on deformation in fault zones. In this first paper of a two-paper set, we focus on the laboratory rock physics aspects of the peak delay analysis. In contrast, a second companion paper presents the theoretical and computational modelling of the inferred processes.

2 Data and Methods

2.1 Material investigated, experimental setup and data acquisition

Known for its homogenous properties, Darley Dale Sandstone (DDS) is a brown-yellow, feldspathic sandstone with a modal composition of quartz (69%), feldspars (26%), clay (3%) and mica (2%). Previous studies report a connected porosity of 13.3% ± 0.8%, with grain sizes varying from 100-800 μm (Heap et al., 2009). No distinct layering or laminations are identified in hand sample. The samples used in this study are 4 cm (diameter) x 10 cm (length) cylinders obtained using a hollow diamond-tipped coring drill with the ends ground flat and parallel to within 0.01mm (King et al., 2020, 2021).

A conventional triaxial deformation cell, installed at the Rock Mechanics Laboratory, University of Portsmouth (e.g., Harnett et al., 2018) deformed the sample. For data acquisition, the protocol of Benson et al. (2007) was followed. The acquisition setup is summarised in **Table 1**. The dry sample was positioned inside a rubber FKM-B nitrile jacket in which an array

of twelve 1MHz Nano-30 (physical acoustics) piezo-electric transducers (PZTs) were embedded. The jacket was then placed inside the deformation cell, and the PZTs were connected to a high-speed digitizer (10 MHz sampling rate) via 60 dB signal preamplifiers. Once sealed, the rubber jacket separates the sample from the oil confining medium, generating a confining pressure of 20 MPa ($\sigma_2 = \sigma_3$). Axial stress, σ_1, is applied via a piston at a constant strain rate of 3.6 mm/h, a strain rate of approximately 10^{-5} s^{-1}. The sample is deformed until a macroscopic fault zone coalesces at dynamic failure.

Table 1: Summary of laboratory acquistion parameters.

Experimental Conditions		Data Acquisition	
Characteristic	Value	Characteristic	Value
Confining Pressure	20 MPa	Sensor Model	PAC Nano30
Strain Rate	10^{-5} s^{-1}	Frequency Sensitivity	1 MHz
Sample Dimensions	40 x 100 mm	Flat Frequency Response	125 - 750 KHz
Sample Shape	Cylinder	Trigger Voltage	60 mV
No. of AE Sensors	12	Preamplifier	60 dB

2.2 Waveform picking and source location

Triggered AE events were recorded when energy exceeded a minimum threshold of 60 mV at any sensor of the 12-channel array. An ASC Richter system (AE recorder) was used for digitising the signals. The P-wave onsets of recorded AE are picked automatically using a Time Delay Neural Network (TDNN) (King et al., 2020; Peddinti et al., 2015; Waibel et al., 1995). A model is trained on time-series of instantaneous frequency (N. E. Huang et al., 1998), seismic amplitude and permutation entropy (Unakafova & Keller, 2013). By applying a binary classification approach of the AE, the waveform can be categorised as either background noise

or signal, providing more efficient time-series to pick the onset of energy even at low amplitudes.

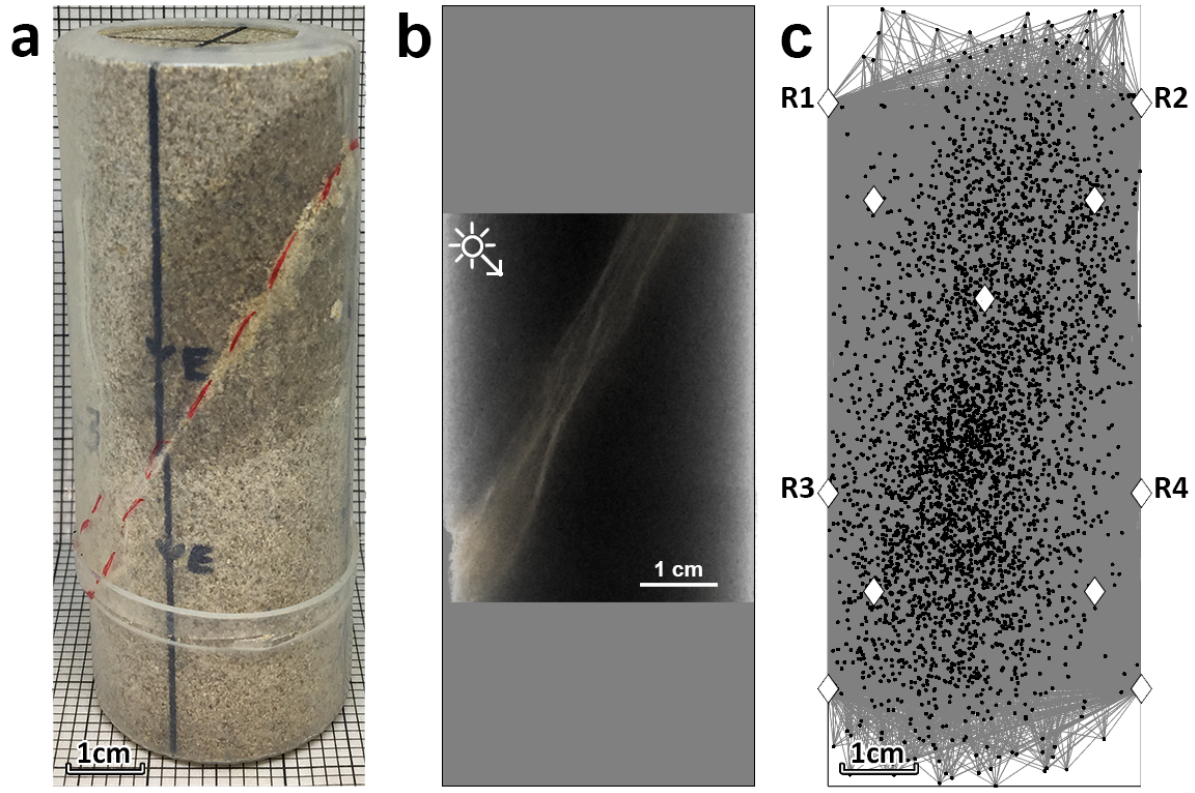

Figure 1: a) Post-deformation imagery highlight surface expressions of fault zone structure (red line). b) Enhanced 3D X-Ray Computed Tomography of the deformed sample with the fault surface highlighted from the northwest. It is not perfectly planar and deviates from a flat surface by up to 4 mm in either direction. The bounding box indicates sample boundaries. c) Source locations (black dots), ray paths (assumed straight, grey lines) and receiver array geometry (diamonds).

A Time Difference of Arrival method (TDOA) is applied to locate the AE epicentres using P-wave onsets (Comanducci et al., 2020; Tobias, 1976). Pairwise subtraction of observed arrival times (a minimum of 6) to each sensor is minimised against calculated arrivals times through iterative estimation of the source location. The L2 norm arrives at a local minimum at the source location with a maximum estimated error of 2 mm. In post-deformation imagery, simple surface expressions of fractures highlight newly formed fault zone structure dipping 60° to the left following sample failure (dashed red line, **Figure 1a**). Enhanced X-ray Computed Tomography highlights the single failure plane illuminated from the northwest (**Figure 1b**). We note that this is not a perfectly planar feature, deviating from a flat surface by

approximately 4 mm in either direction. PZT receivers (diamonds), source locations (black circles) and straight ray paths (grey lines) indicate that the AE waveforms have extensively sampled the deformation structure (**Figure 1c**).

The source mechanism could dominate the waveform and thus peak delays at such small hypocentral distances. For example, variations in frequency content have been previously used for source classification (Ohtsu et al., 2002). In addition, discrepancies in the attenuation properties of tensile events have been related to the orientation of the fault (Kwiatek & Ben-Zion, 2013). Following the methodology of King et al. (2021), the radiation patterns of AE were classified to determine source-specific variations character and frequency content. Fracturing mechanisms fall within a range of distributions whose extremes are pure compaction (C-type), pure shear (S-type) and pure tension (T-Type) (Frohlich et al., 2016; King et al., 2021).

Near-source scattering results in increased complexity of the direct wave energy when an event occurs close to a boundary or discontinuity (Lacanna & Ripepe, 2013); in this case, strong P-wave reflections can modify early S-wave amplitudes. Unclear S-wave onsets were picked automatically, following a time-frequency transformation of the signal (Constant-Q Transform, CQT). The CQT is a technique that transforms a time-domain signal into the time-frequency domain with non-stationary Gabor frames. The centre frequencies of the frequency bins are logarithmically spaced, and their Q-factors are all equal. It is essentially a wavelet transform with a higher potential resolution than conventional techniques (12-96 bins per octave). The Q-factor of bin k is defined $Q_k = \frac{f_k}{\Delta f_k} = \frac{N_k f_k}{\Delta \omega f_s}$, where f_k, Δf_k and $\Delta \omega f_s$ denote the centre frequency, the -3 dB bandwidth of the frequency response and the -3 dB bandwidth of the main lobe of the spectrum of the window function, respectively (Schörkhuber & Klapuri, 2010). The window length N_k is inversely proportional to f_k to have the same Q-factor for each bin. After

computing the highest octave Q-factors over the entire signal, the input is lowpass filtered and downsampled by a factor of 2 to repeat the calculation for the desired number of octaves (Schörkhuber and Klapuri, 2010). The S-wave onset is then defined as a local minimum in the CQT of the waveform bandpass filtered between 300 and 600 kHz, occurring shortly after the first pulse of the P-wave. Due to the near-source scattering effects, it is not reliable to separate reflected P-wave energy from the S-wave; therefore, this onset is defined as "Beyond the Direct Wave" (BYD).

2.3 AE source mechanisms, ray paths and waveforms

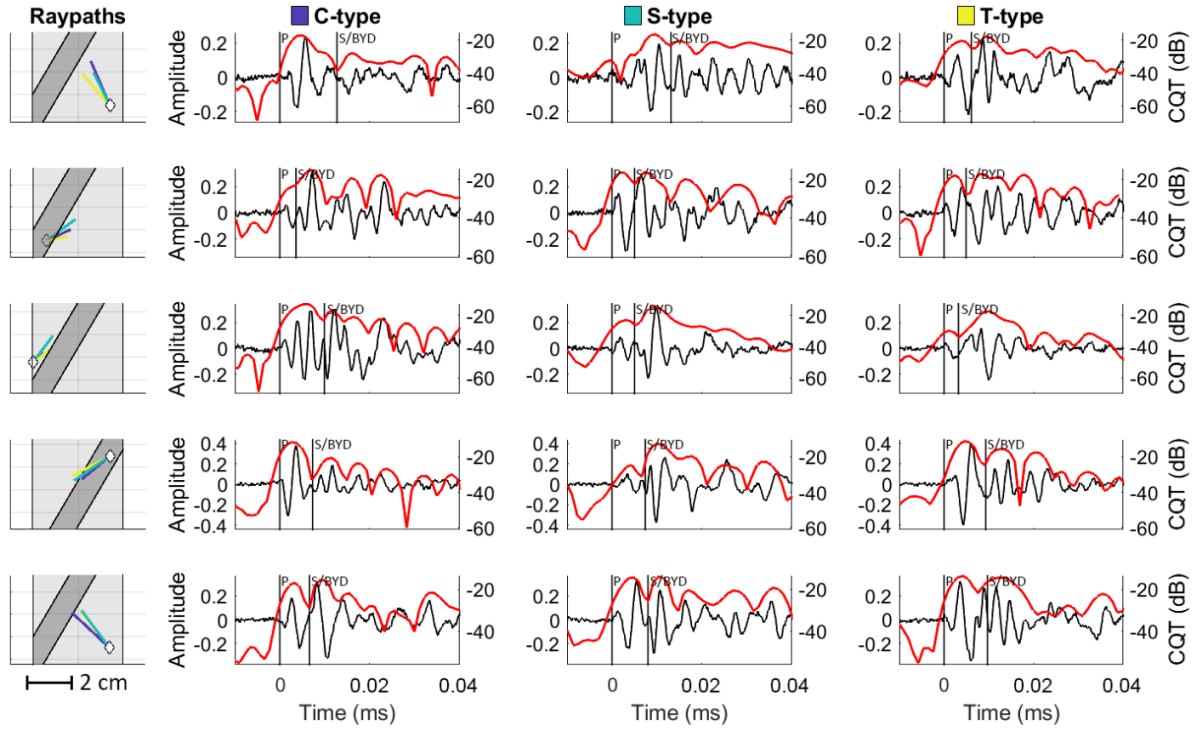

Figure 2: Example waveforms for each mechanism type (columns) occurring close to each other in space and time (rows). The first column indicates ray paths (coloured lines corresponding to mechanism type) of events to a receiver (diamond). A dark grey region is used to indicate the fault zone. Waveforms are presented with their corresponding Constant-Q Transform (red line), used to estimate the "beyond the direct wave" onset.

Only the first arriving waveform for AE is considered to determine what waveform attributes are related to the source (**Figure 2**). These typically only travel 1-2 cm before reaching a receiver. Waveforms were selected from AE located within 12.5 mm of each other (approximately one wavelength at 200 kHz) and that occurred within a 2-minute window. This

selection minimised the influence of time-varying structures whilst ensuring a representative from each mechanism type (**Figure 2**, columns 2-4). Waveforms are presented with corresponding ray paths (**Figure 2**, column 1, coloured lines) and the CQT that defines the BYD onset (**Figure 2**, columns 2-4, red line). Vertical black lines indicate P-wave and estimated BYD arrivals.

Path-dependent effects dominate the waveform from the early onset, and it is difficult to discriminate the properties of the different source types. Individual waveforms for each mechanism are averaged together and are presented with the bootstrapped modal frequency content (Hilbert transform, **Figure 3**, bottom row). The grey regions indicate the standard deviation (1 std and 1/5 std) of the bootstrapped time series, and *n* is the number of waveforms. Vertical black bars indicate the average P-wave and BYD arrival times. Here, the BYD shows an approximate 30 kHz reduction in dominant frequency content, regardless of mechanism type. However, high amplitude reflections from near-source scattering overlap these arrivals (e.g., BYD, **Figure 3**, top row). Additional reflections arrive approximately 0.02 ms after the P-wave onset, likely caused by interaction with the sample boundaries. The three mechanisms produce small differences in the BYD estimation and, therefore, the corresponding peak delay measurement.

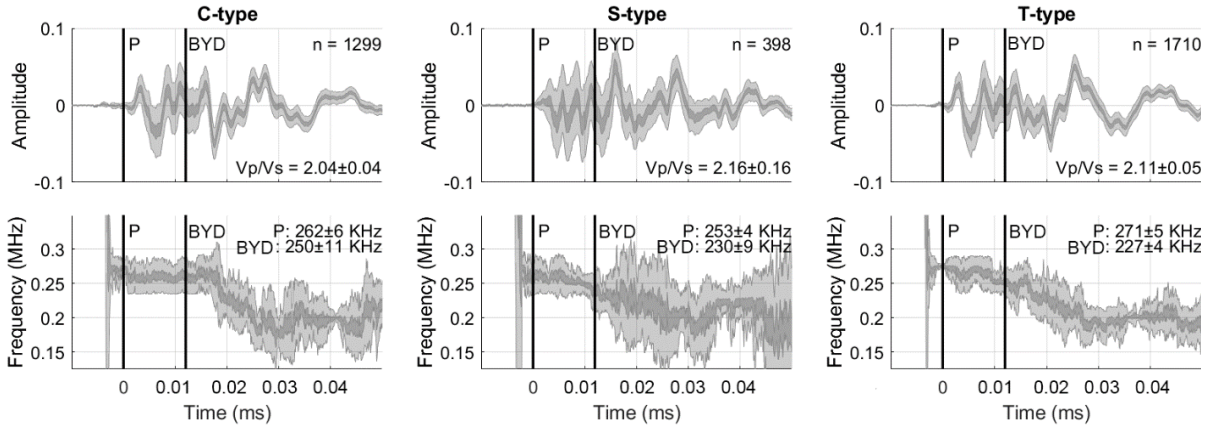

Figure 3: Average waveform and dominant frequency content for *n* waveforms. Vertical bars indicate average P-wave and S/BYD onsets for DDS.

2.4 Measuring peak delay at the laboratory scale

Relative to the field scale, laboratory media show higher levels of heterogeneity. Consequently, scattering might evolve from the Rayleigh (at low frequencies) to the Mie (at higher frequencies) scattering regime. Therefore, peak delays were measured on waveforms filtered in two frequency bands: 0.05-0.5 MHz and 0.5-1 MHz. Assuming a typical S-wave velocity of 2.3 km/s (Heap et al., 2009), this corresponds to wavelengths of 44.6 mm (0.05 MHz), 4.5 mm (0.5 MHz) and 2.2 mm (1 MHz). The low-frequency observations thus fall within the near-field Rayleigh scattering, while the high frequencies are dominated by far-field Mie scattering. PZT receivers orthogonal to the developing fault zone are investigated in further detail in the following sections (**Figure 1c**, R1-R4).

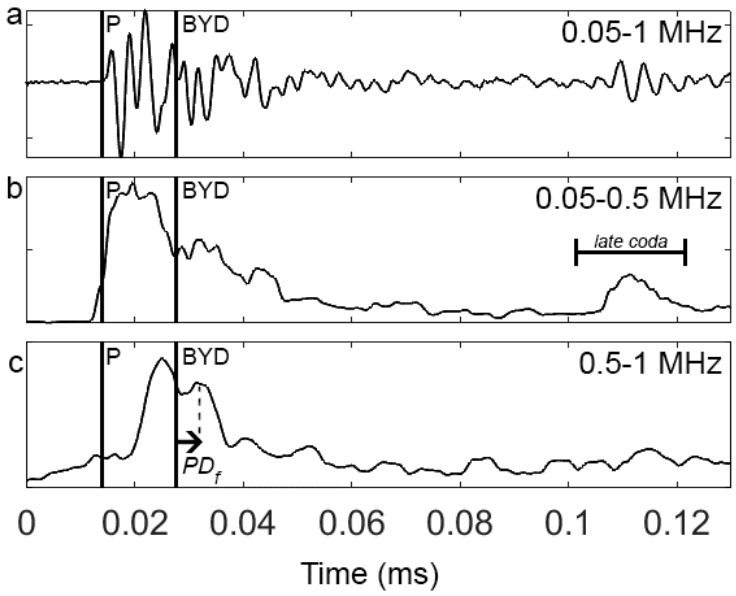

Figure 4: Example of observed AE and its envelopes. a) Displacement voltage waveform in 0.05-1 MHz band. P-wave and BYD onsets are indicated. b) RMS envelope at 0.05-0.5 MHz. A late coda arrival occurs for many waveforms between 0.1 and 0.12 ms. c) RMS envelope at 0.5-1 MHz. PD_f is the peak delay time from the BYD onset.

A generalised definition of the relative variation of peak delay is proposed in Takahashi et al. (2007) to account for a travel-time dependence that occurs at the far-field. However, De Siena et al. (2016) noted that high uncertainties affect the coefficients obtained in the proposed linear

model, and the fit is imprecise for short hypocentral distances. Further, Zhang et al. (2019) concluded that the traditional exponential function models of attenuation laws are insufficient to describe the amplitude losses of AE waves in the near field. Therefore, unlike field-scale studies, we do not consider the influence of hypocentral distances in this study. A peak delay is defined here as the time difference between the BYD onset and the maximum amplitude arrival of energy in the coda, to minimise the influence of source/near-source effects. Each signal is filtered in the target frequency band, from which the root mean square (RMS) envelope is calculated (**Figure 4**). Envelopes are smoothed over a 0.005 ms window. Hereafter, peak delay is thus only considered as the relative value $\Delta log\left(PD_f\right)$ that varies around the average of all (n number) measurements for each frequency band (f):

$$\Delta log\left(PD_f\right) = log\left(PD_f\right) - \frac{1}{n}\sum_{i=1}^{n} log\left(PD_f\right).$$

While the definition is analogous to the one used at the field-scale, the parameter is not a measurement of forward scattering modelled by the Markov approximation (e.g., Saito et al. 2002). Our primary hypothesis is that peak delay is a cumulative parameter that cannot be reduced, even if along the ray path there are weak heterogeneities (Takahashi et al., 2007). A small $\Delta\log\left(PD_f\right)$ marks the absence of high heterogeneity along the ray-path while the opposite is true for high values.

3 Results

We present the changes in AE data amplitude, frequency, and peak delay in **Figure 5**. On the left side, we show the probability of detecting AE data of different types during the experiment for different receivers and azimuths (rows). The AE waveforms are categorised according to (1) frequency and (2) amplitude contents in the late coda as either *high* or *low*. The threshold is at 50% of the range for each parameter throughout the experiment. Thus, we can define four groups: (1) low frequency, low amplitude coda (LF-LA), (2) low frequency, high amplitude

coda (LF-HA), (3) high frequency, low amplitude coda (HF-LA) and (4) high frequency, high amplitude coda (HF-HA). For each category, a probability density function (PDF) is calculated for the time of occurrence of individual waveforms as a function of time. All four PDFs are then summed together, and a percentage contribution is calculated (King et al., 2021). In **Figure 5** (right), the $\Delta\log(PD_f)$ values are presented with smoothed trends and linear fits weighted according to the number of measurements in a moving window of ~10 seconds between 20 and 40 minutes (experiment time).

When considering arrivals to all the PZT receivers (**Figure 5a**), the first half of the experiment is dominated by LF energy, likely related to the generation of surface waves from the sample boundaries (Yoshimitsu et al., 2016). A family of HF-LA events rapidly reduces in probability from >40% to almost <5% during the first 10 minutes. These events are notably absent from the off-fault station (**Figure 5c**), even if interpreting this period is challenging as the sampling is low. After this time, HF events steadily increase as new fractures nucleate. As the fault zone begins to coalesce at ~25 minutes, the number of AE rapidly increases, and a new group of HF-HA events starts to dominate. These events have an occurrence likelihood of >40% at sample failure. Considering the geometrical trade-off imposed by the relative source-fault-receiver pathways, these waveforms arrive primarily to the on-fault receiver (**Figure 5b**) with little-to-no arrivals for the off-fault station (**Figure 5c**). These differences affect the peak delay measurement at on-fault stations, where a gradual increase in peak delay is observed for both frequency bands. The opposite happens at off-fault stations, where a decreasing trend is visible.

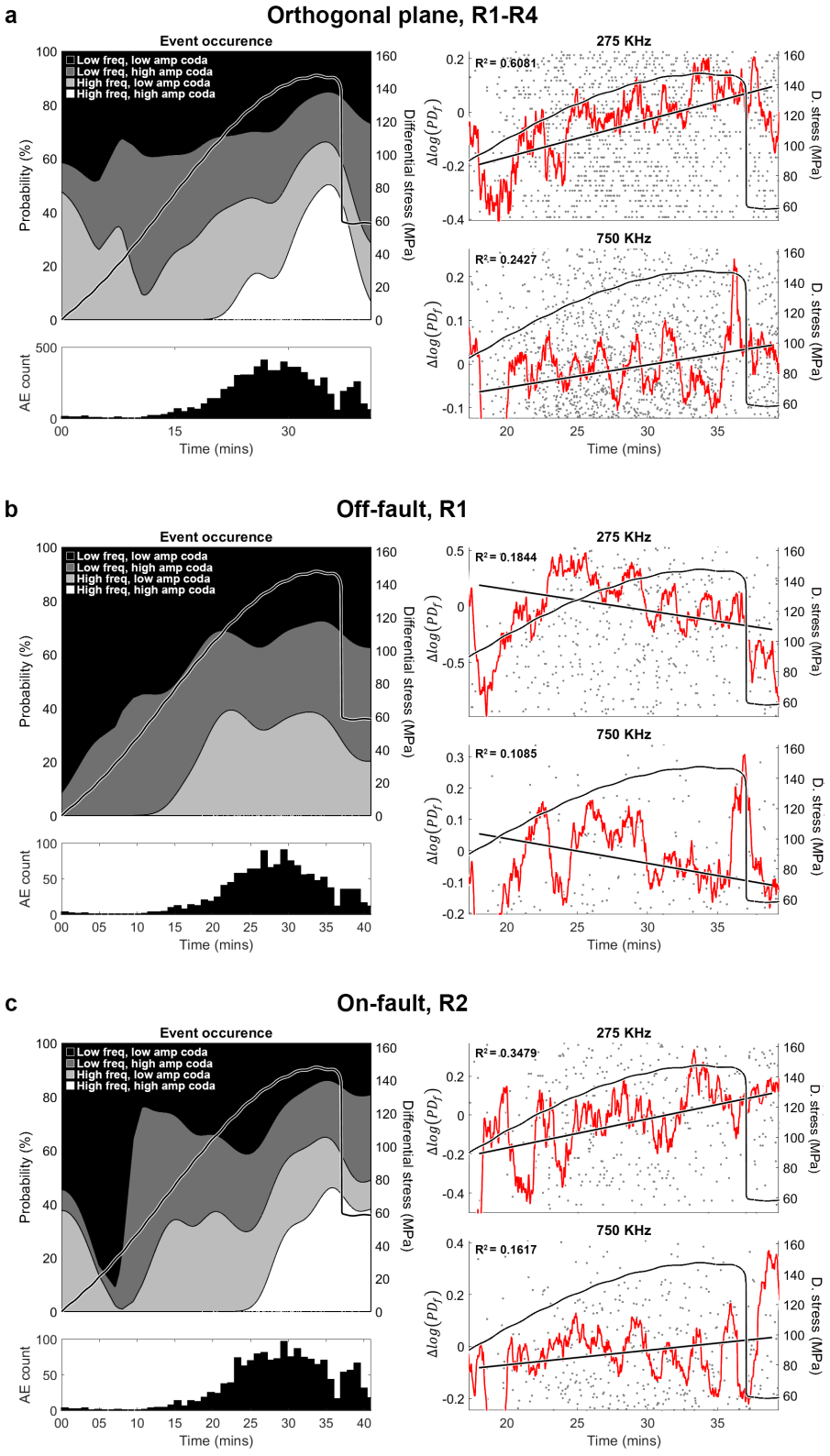

Figure 5: Time-dependent variations in frequency and amplitude content of the AE coda for a) arrivals to orthogonal receivers R1-R4, b) arrivals to on-fault receiver R2 and c) arrivals to off-fault receiver R1. In each case, the left panels show (1) the probability, or ratio, of the four groups relative to total; (2) histogram counts of AE data. Right panels show true (dots, incomplete due to spread), smoothed (red) and linear fit of $\Delta\log(PD_f)$ for the analysed frequency bands (right).

In analogy to field-scale tomography, the medium is discretised into model blocks (5x5x5 mm in size) to obtain an image of the interior of the sample. The model is orientated so that the grid bisects the fault at an orthogonal angle. Each block is assigned the average $\Delta\log(PD_f)$ of all the ray paths that cross it to minimise time-dependent effects (De Siena et al., 2016). Source-receiver pathways are then assigned their measured peak delays. Only blocks crossed by a minimum of 5 rays are solved to minimise anomalous variations in regions of low path coverage. Peak delay values are smoothed at a block by averaging each block-value with blocks within 5 mm distance. The 3D distribution of anomalies is then "depth-averaged" along the fault strike to create a 2D map. Although this approach limits the detection of minor anomalies, it ensures that major structures are adequately sampled from all directions.

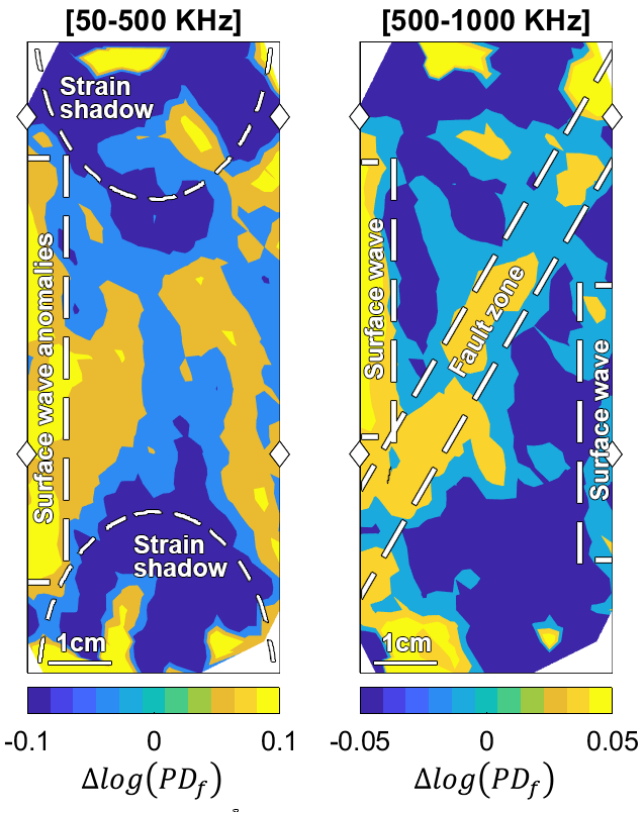

Figure 6: Distribution of logarithmic variations of BYD ($\Delta\log(PD_f)$) obtained using all 12 receivers. The bounding box indicates sample boundaries. Receivers R1-4 are shown as diamonds.

Low-frequency observations show no clear signature of the post-deformation fault zone (**Figure 6**, left). The primary positive peak-delay anomaly underlines the left side of the sample

in both frequency bands (**Figure 6**). A similar anomaly is expected at these frequencies, as the sample boundaries produce surface waves generated by multiple scattering that propagate vertically (Yoshimitsu et al., 2016). The difference in peak intensity is likely related to the proximity of the largest seismicity cluster to the left side of the sample (**Figure 1c**). The result is an increase in the number and energy of reverberating waves. Although the distribution of anomalies suggests strain-forbidden zones at 0.05-0.5 MHz (e.g., Ji & Wang, 2011), there are geometrical trade-offs imposed by the distribution of AE along the fault zone.

The fault-zone is visible as a central, left-dipping region of positive $\Delta\log(PD_f)$ anomalies in the 0.5-1 MHz map (**Figure 6**, right). These anomalies appear to "thicken" towards the lower half of the fault zone, likely due to the observed undulations of the fault surface (**Figure 1b**). Likely, the high values of $\Delta\log(PD_f)$ present along the radial boundaries are again related to surface waves from waveforms that travel along the sample edges (Yoshimitsu et al., 2016). These anomalies are approximately one wavelength in thickness and are similar in magnitude to those produced by the fault zone.

4 Discussion

In regions of strong deformation, the delay in the maximum arrival of seismic energy has been observed to correlate strongly with the distribution of heterogeneity in the lithosphere (Takahashi et al., 2007; De Siena et al., 2016; Napolitano et al., 2020). By adopting standard approaches of scattering (peak delay) tomography, the results presented here suggest that similar processes may occur at the laboratory scale. They highlight a clear potential for AE-led studies to calibrate time-dependent scattering structures like active fault zones (**Figure 5**). Unlike seismic data, which typically sample structures that may change over a few decades (Napolitano et al., 2019), the nature of the laboratory setup results in significant structural variations that can occur over seconds (Benson et al., 2010).

Uncertainties in the frequency characteristics of the source present further trade-offs that require a preliminary characterisation of the source processes (**Figure 4**). Whilst pure shear-type events are likely in the minority (McBeck et al., 2019; Renard et al., 2019a), the source classification routine applied here does not fully account for the frequency drop associated with individual components of shear within dominantly tensile events (King et al., 2021). We have applied large frequency windows and an automated routine to target energies that arrive after the direct wave to minimise such effects on our observations (**Figure 2**).

The low-frequency image replicates: (1) the expected cone-shaped strain-forbidden zones near the pistons where practically no crystal plastic deformation occurs as low peak delays; (2) the combined intense strain and intrusion zones of high and average deformation (**Figure 6**). These zones are expected for viscosity ratios as small as ten between inclusions and surrounding material (Moulas et al., 2014), which is certainly the case in our experiment. However, Yoshimitsu et al. (2016) carried out an experiment on undeformed, homogeneous aluminium samples, showing that surface waves from the sample boundaries can dominate the maps obtained at low frequencies. The variations in the late waveform coda for individual AE confirm the occurrence of LF-HA arrivals approximately 0.1 ms after the P-wave (**Figure 4**). We will test this trade-off in the companion paper (this volume, K22B). Guture experiments on different samples could confirm that peak delays are sensitive to deformation-induced heterogeneity in this frequency band and at this scale, even if they have no resolution on the shear zone. This confirmation is essential to link the seismic response to metamorphic processes triggered by increasing heterogeneity (Moulas et al., 2014; Cioniu et al., 2019). These processes are not limited to this scale of investigation.

Less uncertainty affects the high-frequency imaging, where the shear zone is visible as high peak delays. Pore space topology alone can play an essential role in increasing peak delays of high-frequency waveforms (Di Martino et al., 2021); therefore, similar mechanisms likely

occur in this fractured fault-driven system. We further investigate this relationship between frequency and fault structure in the companion study (this volume, K22B). Despite the limitations in observation geometry, the maps in **Figure 6** indicate that peak delays can map strain-related structures (**Figure 1**).

The time-dependent results indicate that the mapped features are time-dependent, like in field-scale fault zones (Napolitano et al., 2019; Qiu et al., 2020). In **Figure 5**, we observe a dominance of higher-frequency energy within the coda window as the fault zone coalesces. For on-fault stations, this is driven by a relative increase in the number of HF arrivals in the coda, leading to higher peak delays at higher frequencies (**Figure 5b**). The explanation, tested in the companion study, is that trapped scattered waves in the near-field create these arrivals. For example, these waves have been previously related to field-scale deformation structure (e.g., Qiu et al., 2020; Roy et al., 2020). Power density spectra analysis of fault-zone trapped waves has shown that they maintain larger amplitudes and longer wave trains (therefore higher peak delays) at seismic stations closer to the Longmen Shan fault zone (Y. Huang et al., 2020). For off-fault stations, the observed reduction of peak delay in both frequency bands may be due to attenuation of the surface wave as the fault zone becomes increasingly dominant over sample boundary effects (**Figure 5c**). These results highlight the importance of amplitude information when considering surface wave arrivals that interact with field-scale deformation features characterised by sharp acoustic impedances (Ikeda & Tsuji, 2016).

Our results provide a laboratory-scale calibration to observations made in the field. Nonetheless, due to limitations in sampling and the complexity of the data, a time-dependent peak delay tomography remains impractical. However, a proxy can be realised through numerical simulations of wavefield propagation that assess the different stages of deformation and rupture in fault zones. We perform this numerical analysis in the companion study of this two-paper set (this volume, K22B). Observed waveforms from the laboratory experiment are

used as a target to fit model parameters of stiffness, seismic Q and S-wave velocity during the early phases of deformation and shortly following the dynamic failure of the sample. By linking scattering and dissipation parameters to rough faulting, distributed weakening, and off-fault deformation (Griffith et al., 2010; Renard et al., 2019b), this approach could pave the way for the use of scattering and absorption attributes beyond mapping, e.g., to monitor regions of expected rupture.

5 Conclusions

We developed Acoustic Emission experiments in Darley Dale Sandstone to test the sensitivity of peak delay, a known proxy of seismic scattering at the field scale, to deformation-induced structures, strain, and rheological heterogeneities. We map peak delays in space, obtaining tomographic maps in low (50-500 kHz) and high (500 kHz – 1 MHz) frequency ranges. The results show that peak delays are sensitive to surface waves developing across the boundaries of the sample; however, depending on frequency, they are also sensitive to primary, known spatial variations in heterogeneity and strain. At low frequency, the resolution is sufficient to map differences in strain caused by the heterogeneity of the sample, which is progressively increasing. However, the enhancement of surface waves from the sample boundary could trade off with the observation. At high frequencies, peak delays detect the zone of intense strain corresponding to the post-deformation shear zone. Temporal analysis confirms a dependence of peak delays on the different stages of deformation. However, the trends depend on the position of source and sensor, with the highest peak delays appearing at sensors in contact with the developing shear zone.

Peak delays are essential for assessing earthquake source characteristics and are now used for imaging the heterogeneous Earth in combination with coda parameters, specifically coda attenuation. The sensitivity to heterogeneity, strain, and fracturing, shown by peak delay

imaging and temporal variations is key for assessing their potential for mapping damage in the Earth's crust. The results presented here provide invaluable constraints to interpret field-scale parameters. Together with our companion modelling paper, which offers necessary physical explanations to our results, the present work has important implications for field-scale measurements and imaging of scattering parameters, especially in the near-source high-scattering regime.

6 References

Adam, L., Batzle, M., Lewallen, K. T., & van Wijk, K. (2009). Seismic wave attenuation in carbonates. *Journal of Geophysical Research: Solid Earth*, *114*(B6).

Barnhoorn, A., Verheij, J., Frehner, M., Zhubayev, A., & Houben, M. (2018). Experimental identification of the transition from elasticity to inelasticity from ultrasonic attenuation analysesAttenuation and the onset of inelasticity. *Geophysics*, *83*(4), MR221–MR229.

Baud, P., & Meredith, P. (1997). Damage accumulation during triaxial creep of Darley Dale sandstone from pore volumometry and acoustic emission. *International Journal of Rock Mechanics and Mining Sciences*, *34*(3–4), 24-e1.

Benson, P. M., Thompson, B. D., Meredith, P. G., Vinciguerra, S., & Young, R. P. (2007). Imaging slow failure in triaxially deformed Etna basalt using 3D acoustic-emission location and X-ray computed tomography. *Geophysical Research Letters*, *34*(3). https://doi.org/10.1029/2006gl028721

Benson, P. M., Vinciguerra, S., Meredith, P. G., & Young, R. P. (2010). Spatio-temporal evolution of volcano seismicity: A laboratory study. *Earth and Planetary Science Letters*, *297*(1–2), 315–323.

Bianco, F., Pezzo, E. D., Malagnini, L., Luccio, F. D., & Akinci, A. (2005). Separation of depth-dependent intrinsic and scattering seismic attenuation in the northeastern sector of the Italian Peninsula. *Geophysical Journal International*, *161*(1), 130–142.

Borleanu, F., De Siena, L., Thomas, C., Popa, M., & Radulian, M. (2017). Seismic scattering and absorption mapping from intermediate-depth earthquakes reveals complex tectonic interactions acting in the Vrancea region and surroundings (Romania). *Tectonophysics*, *706–707*, 129–142. https://doi.org/10.1016/j.tecto.2017.04.013

Calvet, M., Sylvander, M., Margerin, L., & Villaseñor, A. (2013). Spatial variations of seismic attenuation and heterogeneity in the Pyrenees: Coda Q and peak delay time analysis. *Tectonophysics*, *608*, 428–439. https://doi.org/10.1016/j.tecto.2013.08.045

Carcione, J. M., & Picotti, S. (2006). P-wave seismic attenuation by slow-wave diffusion: Effects of inhomogeneous rock properties. *Geophysics*, *71*(3), O1–O8.

Chapman, M. (2003). Frequency-dependent anisotropy due to meso-scale fractures in the presence of equant porosity. *Geophysical Prospecting*, *51*(5), 369–379.

Cionoiu, S., Moulas, E., & Tajčmanová, L. (2019). impact of interseismic deformation on phase transformations and rock properties in subductions zone. *Scientific Reports*, *9*(1), 1–6.

Comanducci, L., Cobos, M., Antonacci, F., & Sarti, A. (2020). Time Difference of Arrival Estimation from Frequency-Sliding Generalized Cross-Correlations Using

Convolutional Neural Networks. In *ICASSP 2020-2020 IEEE International Conference on Acoustics, Speech and Signal Processing (ICASSP)* (pp. 4945–4949). IEEE.

De Siena, L., Calvet, M., Watson, K. J., Jonkers, A. R. T., & Thomas, C. (2016). Seismic scattering and absorption mapping of debris flows, feeding paths, and tectonic units at Mount St. Helens volcano. *Earth and Planetary Science Letters*, *442*, 21–31. https://doi.org/10.1016/j.epsl.2016.02.026

Di Martino, M. D. P., De Siena, L., Healy, D., & Vialle, S. (2021). Petro-mineralogical controls on coda attenuation in volcanic rock samples. *Geophysical Journal International*, *226*(3), 1858–1872.

Durán, E. L., van Wijk, K., Adam, L., & Wallis, I. C. (2018). Separating intrinsic and scattering attenuation in full waveform sonic logging with radiative transfer theory. *Geophysical Journal International*, *213*(2), 757–769.

Fang, X., Fehler, M., Chen, T., Burns, D., & Zhu, Z. (2013). Sensitivity analysis of fracture scattering. *GEOPHYSICS*, *78*(1), T1–T10. https://doi.org/10.1190/geo2011-0521.1

Fehler, M. (1991). Numerical basis of the separation of scattering and intrinsic absorption from full seismogram envelope. A monte-carlo simulation of multiple isotropic scattering. *Papers in Meteorology and Geophysics*, *42*(2), 65–91.

Frohlich, C., DeShon, H., Stump, B., Hayward, C., Hornbach, M., & Walter, J. I. (2016). A historical review of induced earthquakes in Texas. *Seismological Research Letters*, *87*(4), 1022–1038.

Griffith, W. A., Nielsen, S., Di Toro, G., & Smith, S. A. (2010). Rough faults, distributed weakening, and off-fault deformation. *Journal of Geophysical Research: Solid Earth*, *115*(B8).

Harnett, C. E., Benson, P. M., Rowley, P., & Fazio, M. (2018). Fracture and damage localization in volcanic edifice rocks from El Hierro, Stromboli and Tenerife. *Scientific Reports*, *8*(1). https://doi.org/10.1038/s41598-018-20442-w

Heap, M. J., Baud, P., Meredith, P. G., Bell, A. F., & Main, I. G. (2009). Time-dependent brittle creep in Darley Dale sandstone. *Journal of Geophysical Research: Solid Earth*, *114*(B7).

Huang, N. E., Shen, Z., Long, S. R., Wu, M. C., Shih, H. H., Zheng, Q., et al. (1998). The empirical mode decomposition and the Hilbert spectrum for nonlinear and non-stationary time series analysis. *Proceedings of the Royal Society of London. Series A: Mathematical, Physical and Engineering Sciences*, *454*(1971), 903–995.

Huang, Y., Li, H., Liu, X., Zhang, Y., Liu, M., Guan, Y., & Su, J. (2020). The Multiscale Structure of the Longmen Shan Central Fault Zone from Local and Teleseismic Data Recorded by Short-Period Dense Arrays. *Bulletin of the Seismological Society of America*, *110*(6), 3077–3087. https://doi.org/10.1785/0120190292

Ikeda, T., & Tsuji, T. (2016). Surface wave attenuation in the shallow subsurface from multichannel–multishot seismic data: a new approach for detecting fractures and lithological discontinuities. *Earth, Planets and Space*, *68*(1), 111. https://doi.org/10.1186/s40623-016-0487-0

Imperatori, W., & Mai, P. M. (2015). The role of topography and lateral velocity heterogeneities on near-source scattering and ground-motion variability. *Geophysical Journal International*, *202*(3), 2163–2181.

Ji, S., & Wang, Q. (2011). Interfacial friction-induced pressure and implications for the formation and preservation of intergranular coesite in metamorphic rocks. *Journal of Structural Geology*, *33*(2), 107–113.

King, T., Benson, P., De Siena, L., & Vinciguerra, S. (2020). Acoustic Emission Waveform Picking with Time Delay Neural Networks during Rock Deformation Laboratory Experiments. *Seismological Research Letters*. https://doi.org/10.1785/0220200188

King, T., Vinciguerra, S., Burgess, J., Benson, P., & Siena, L. D. (2021). Source Mechanisms of Laboratory Earthquakes During Fault Nucleation and Formation. *Journal of Geophysical Research: Solid Earth*, *126*(5), e2020JB021059. https://doi.org/10.1029/2020JB021059

Kwiatek, G., & Ben-Zion, Y. (2013). Assessment of P and S wave energy radiated from very small shear-tensile seismic events in a deep South African mine. *Journal of Geophysical Research: Solid Earth*, *118*(7), 3630–3641. https://doi.org/10.1002/jgrb.50274

Lacanna, G., & Ripepe, M. (2013). Influence of near-source volcano topography on the acoustic wavefield and implication for source modeling. *Journal of Volcanology and Geothermal Research*, *250*, 9–18. https://doi.org/10.1016/j.jvolgeores.2012.10.005

Maercklin, N., Haberland, C., Ryberg, T., Weber, M., & Bartov, Y. (2004). Imaging the Dead Sea Transform with scattered seismic waves. *Geophysical Journal International*, *158*(1), 179–186.

Main, I. G., Peacock, S., & Meredith, P. G. (1990). Scattering attenuation and the fractal geometry of fracture systems. *Pure and Applied Geophysics*, *133*(2), 283–304.

McBeck, J., Kandula, N., Aiken, J. M., Cordonnier, B., & Renard, F. (2019). Isolating the factors that govern fracture development in rocks throughout dynamic in situ X-ray tomography experiments. *Geophysical Research Letters*.

Moulas, E., Burg, J. P., & Podladchikov, Y. (2014). Stress field associated with elliptical inclusions in a deforming matrix: Mathematical model and implications for tectonic overpressure in the lithosphere. Tectonophysics, 631, 37-49.

Napolitano, F., De Siena, L., Gervasi, A., Guerra, I., Scarpa, R., & La Rocca, M. (2019). Scattering and absorption imaging of a highly fractured fluid-filled seismogenetic volume in a region of slow deformation. *Geoscience Frontiers*. https://doi.org/10.1016/j.gsf.2019.09.014

Ohtsu, M., Uchida, M., Okamoto, T., & Yuyama, S. (2002). Damage Assessment of Reinforced Concrete Beams Qualified by Acoustic Emission. *Structural Journal*, *99*(4), 411–417. https://doi.org/10.14359/12109

Peddinti, V., Chen, G., Manohar, V., Ko, T., Povey, D., & Khudanpur, S. (2015). Jhu aspire system: Robust lvcsr with tdnns, ivector adaptation and rnn-lms. In *2015 IEEE Workshop on Automatic Speech Recognition and Understanding (ASRU)* (pp. 539–546). IEEE.

Qiu, H., Allam, A. A., Lin, F.-C., & Ben-Zion, Y. (2020). Analysis of Fault Zone Resonance Modes Recorded by a Dense Seismic Array Across the San Jacinto Fault Zone at Blackburn Saddle. *Journal of Geophysical Research: Solid Earth*, *125*(10), e2020JB019756.

Rao, Y., & Wang, Y. (2009). Fracture effects in seismic attenuation images reconstructed by waveform tomography. *GEOPHYSICS*, *74*(4), R25–R34. https://doi.org/10.1190/1.3129264

Renard, F., McBeck, J., Kandula, N., Cordonnier, B., Meakin, P., & Ben-Zion, Y. (2019a). Volumetric and shear processes in crystalline rock approaching faulting. *Proceedings of the National Academy of Sciences*, *116*(33), 16234–16239. https://doi.org/10.1073/pnas.1902994116

Renard, F., McBeck, J., Kandula, N., Cordonnier, B., Meakin, P., & Ben-Zion, Y. (2019b). Volumetric and shear processes in crystalline rock approaching faulting. *Proceedings of the National Academy of Sciences*, *116*(33), 16234–16239.

Ripperger, J., Mai, P. M., & Ampuero, J.-P. (2008). Variability of near-field ground motion from dynamic earthquake rupture simulations. *Bulletin of the Seismological Society of America*, *98*(3), 1207–1228.

Roy, N., Mukherjee, S., & Sahu, R. B. (2020). Influence of trapped soft/stiff soil layer in seismic site response analysis. *Journal of Earth System Science*, *129*(1), 1–19.

Saito, T. (2002). Envelope broadening of spherically outgoing waves in three-dimensional random media having power law spectra. *Journal of Geophysical Research*, *107*(B5). https://doi.org/10.1029/2001jb000264

Schörkhuber, C., & Klapuri, A. (2010). Constant-Q transform toolbox for music processing. In *7th Sound and Music Computing Conference, Barcelona, Spain* (pp. 3–64).

Schubnel, A., Nishizawa, O., Masuda, K., Lei, X. J., Xue, Z., & Guégen, Y. (2003). Velocity Measurements and Crack Density Determination During Wet Triaxial Experiments on Oshima and Toki Granites. *Pure and Applied Geophysics*, *160*(5), 869–887. https://doi.org/10.1007/pl00012570

Sketsiou, P., Napolitano, F., Zenonos, A., & De Siena, L. (2020). New insights into seismic absorption imaging. *Physics of the Earth and Planetary Interiors*, *298*, 106337.

Takahashi, T., Sato, H., Nishimura, T., & Obara, K. (2007). Strong inhomogeneity beneath Quaternary volcanoes revealed from the peak delay analysis ofS-wave seismograms of microearthquakes in northeastern Japan. *Geophysical Journal International*, *168*(1), 90–99. https://doi.org/10.1111/j.1365-246x.2006.03197.x

Takahashi, T., Sato, H., Nishimura, T., & Obara, K. (2009). Tomographic inversion of the peak delay times to reveal random velocity fluctuations in the lithosphere: method and application to northeastern Japan. *Geophysical Journal International*, *178*(3), 1437–1455. https://doi.org/10.1111/j.1365-246x.2009.04227.x

Tisato, N., & Quintal, B. (2014). Laboratory measurements of seismic attenuation in sandstone: Strain versus fluid saturation effectsStrain and saturation effects. *Geophysics*, *79*(5), WB9–WB14.

Tobias, A. (1976). Acoustic-emission source location in two dimensions by an array of three sensors. *Non-Destructive Testing*, *9*(1), 9–12. https://doi.org/10.1016/0029-1021(76)90027-X

Tripathi, J. N., Sato, H., & Yamamoto, M. (2010). Envelope broadening characteristics of crustal earthquakes in northeastern Honshu, Japan. *Geophysical Journal International*, *182*(2), 988–1000. https://doi.org/10.1111/j.1365-246x.2010.04657.x

Unakafova, V., & Keller, K. (2013). Efficiently measuring complexity on the basis of real-world data. *Entropy*, *15*(10), 4392–4415.

Vlastos, S., Liu, E., Main, I. G., & Narteau, C. (2007). Numerical simulation of wave propagation in 2-D fractured media: scattering attenuation at different stages of the growth of a fracture population. *Geophysical Journal International*, *171*(2), 865–880. https://doi.org/10.1111/j.1365-246x.2007.03582.x

Waibel, A., Hanazawa, T., Hinton, G., Shikano, K., & Lang, K. J. (1995). Phoneme recognition using time-delay neural networks. *Backpropagation: Theory, Architectures and Applications*, 35–61.

Yoshimitsu, N., Furumura, T., & Maeda, T. (2016). Geometric effect on a laboratory-scale wavefield inferred from a three-dimensional numerical simulation. *Journal of Applied Geophysics*, *132*, 184–192.

Zhang, G., Li, H., Wang, M., Li, X., Wang, Z., & Deng, S. (2019). Crack-induced acoustic emission and anisotropy variation of brittle rocks containing natural fractures. *Journal of Geophysics and Engineering*, *16*(3), 599–610. https://doi.org/10.1093/jge/gxz031

Mapping Faults in the Laboratory with Seismic Scattering 2: The Modelling Perspective

Key Points:

- Isotropic modelling of ultrasonic scattering measurements in a deformed rock sample.
- Simulation of peak delays, low-frequency dissipation, and coda waveforms before and after failure.
- Calibration for near-source field-scale imaging of fracture networks with peak delay and coda attenuation.

Abstract

We mapped peak delays of Acoustic Emission data from rock deformation laboratory experiments. The results suggested that peak delays and, more generally, coda parameters are efficient markers of strain and fracturing. Here, SH waveforms of dominant frequency 200 kHz are forward modelled in a 2D isotropic, layered medium using realistic parameters derived from the laboratory experiments presented in the companion paper (this volume, K22A). The aim is to provide a physical interpretation of the laboratory findings and constrain the role of the evolving fault zone. A 2D fault zone geometry idealising the fracture plane as a more compliant layer was included in the medium, mimicking peak delay mapping and microstructural observations. Measurements of background parameters, as isotropic velocity, and dynamic structures, as fault thickness, were optimised using experimental data and a Genetic Algorithm. Simulations and optimisations clarify that near-source peak delay observations are sensitive to the heterogeneity of zones of intense strain. This sensitivity manifests itself through the arrival of trapped waves within the layer, which couple with multiple reflections from the sample boundaries, visible at off-fault receivers dominated by direct-wave peaks. The highest mapped anomalies in peak delay imaging occur due to measurements at sensors in contact with the inserted layer. When wave propagation crosses the fault, the fault traps and delays waves, which mix with coda. Low-frequency coda develops depending on the relative location of the source, fault, and receiver and is a function of fault width. The 2D simulations prove that peak delays and coda parameters are sensitive to the heterogeneity caused by faulting and strain variations at different stages of fault-inducing slow deformation. These measurements help calibrate field observations suggesting a similar relationship.

1 Introduction

Weak small-scale scattering that perturbs seismic waves in the far field is a standard assumption in seismology. It ensures the applicability of analytical techniques to model seismic wave propagation, allowing us to interpret seismic attributes and image the Earth. In the lithosphere, the delay of the peak energy of high-frequency direct waves is used by a growing number of studies to map spatial variation of seismic scattering (Calvet et al., 2013; Takahashi et al., 2007, 2009). In the far field, seismic scattering is strictly connected to spatial variations of geological units (Borleanu et al., 2017; Calvet et al., 2013). The Markov approximation for spherical waves efficiently models forward scattering of energy for a point source when the

propagation distance (l) is much greater than the scale of heterogeneities (a) and the wavelength (λ) is much shorter than a (Saito, 2002). The Markov approximation thus offers an ideal forward model to image the Earth in these conditions (Takahashi et al., 2009). However, recent studies have detected the complex effects of fault networks and fractured media on peak delay when propagation distances are of the order of a few wavelengths and at the scale of heterogeneity (Napolitano et al., 2019). Imaging with peak delay has become a standard in volcanic settings, where lateral boundary conditions can disperse or trap much of the seismic energy, heavily affecting peak delay measurements depending on frequency (De Siena et al., 2016, 2017; Gabrielli et al., 2020). Nevertheless, the Markov approximation cannot describe wave propagation in the near-field (Sato et al., 2012). No theoretical or experimental framework exists to calibrate scattering and absorption parameters in this distance range and scattering regime.

Acoustic Emissions (AE), the laboratory analogue to seismic data, are used in our companion paper to provide a window into near-field processes that could affect parts of the waveforms where peak delays are measured (this volume, K22A). The heterogeneity in our laboratory experiments is much higher than that assumed in most field studies. For an undeformed Darley Dale Sandstone, a porosity of ~13% results in a typical heterogeneity size of 0.2 mm (Heap et al., 2009). Assuming an average S-wave velocity of 2.23 km/s (Heap et al., 2009), the scattering modelled by simulations will move from quasi-homogeneous or Rayleigh at 150 kHz (ka=0.08) to resonant (Mie) scattering at any frequency above it. As the rock is deformed, compaction of structures leads to an increase of velocity during the pre-failure stages, whilst after failure, there is a marked decrease in the order of 1 km/s (Benson et al., 2007). These inelastic properties are leading physical mechanisms that can be incorporated into models of waveform propagation (Carcione, 2007). Simulations can naturally include anelasticity (e.g., Zhu & Carcione, 2014) whilst also considering many of the physical processes necessary to model attenuation measured from seismic waveforms in complex geological media. Due to the complexity of laboratory samples, it is unlikely to reconstruct all features of the AE waveform without (1) the inclusion of layers or statistical fluctuations in models and (2) considering the spatial relation between source, localised heterogeneity, and sample boundaries. Wave-equation finite-difference simulations can include these effects, targeting the evolution of peak delays through the coda as a marker of scattering.

King et al. 2022a (this volume, K22A) showed that peak delays could identify zones of intense strain in a deforming laboratory sample. The condition is that they are sensitive to fracture

networks and strain-induced heterogeneity in the near field. However, unveiling the exact dependence of peak delays on frequency and fault characteristics from experiments is challenging, as deformation experiments are generally unable to reconstruct high-frequency amplitudes and late arrivals reliably. Depending on confining pressure and frequency, single or coalesced pores, microfractures of varying dimension (Di Martino et al., 2021; Ekanem et al., 2014; Frehner & Schmalholz, 2010; Pyrak-Nolte et al., 1990; Pyrak-Nolte & Nolte, 1992) and rheological heterogeneity (Cionoiu et al., 2019; Ji & Wang, 2011) can all become significant scattering triggers for the seismic wavefield. Synthetic modelling thus becomes the primary tool to understand if peak delays can be used to discriminate on- and off-fault fracturing (Aben et al., 2019) and the onset of fracture coalescence (Stanchits et al., 2006).

In this second part of a two-set study, we model the propagation of AE using the experimental and mapping results presented in K22A, providing a window into the physical processes that lead to frequency- and time-dependent changes in peak delays and coda amplitudes. We focus on peak delay increases and trapped waves resulting from an evolving deformation/shear zone, the dominant processes induced by strain localisation and causing anomalous peak delays, as evidenced in part one. Observed waveforms from the laboratory experiment are used as a target to fit model parameters of stiffness, seismic Q and S-wave velocity during the early phases of deformation and shortly following the dynamic failure of the sample. The fault zone itself is modelled as a single isotropic layer embedded into an isotropic background medium, mimicking the post-fault zone formation mapping. In addition to the inserted layer, simulations consider the partial reflectivity of the finite boundary conditions of the deforming sample as an essential element of the AE waveform. The results provide new insight into relevant processes at the fault scale in the near field.

2 Numerical Method

The impact of developing heterogeneity leading to phase and amplitude variations of horizontally-polarised S-(SH) waveforms is modelled using the literature and data from the deformation experiment of Darley Dale Sandstone (DDS). The 4 x 10 cm sample is deformed until dynamic failure under conventional triaxial conditions at a confining pressure of 20 MPa. An array of 1 MHz Piezo-Electric Transducers (PZT) detect fracturing events as AE throughout the test. These sensors record the stress-displacement field as changes in the output voltage at a 10 MHz resolution. Please refer to K22A for more details on the experimental setup and process.

The modelled acoustic waves propagate at a dominant frequency (f) of 200 kHz, where correlation lengths and waveform distortion are linked to heterogeneity. In K22A, we could not reconstruct the shear zone exactly around this frequency. Still, apparently, high peak delays could define the expected zones of combined high and average strain-induced heterogeneity in the sample. There are no specific experimental measurements of correlation lengths in DDS (a_S), so we use the correlation length established by Nishizawa & Fukushima (2008) for heterogeneous media. We thus assume a correlation length for sandstone of a_S=0.1 mm. In DDS, an S-wave velocity of 2.23 km/s leads to wavelengths between 3.7 mm (600 kHz) and 11.2 mm (200 kHz) (Heap et al., 2009). For any AE event, this means that waves will propagate into the sample from 8 λ (600 kHz) to 3 λ (200 kHz), respectively. In both cases, we are outside the small scattering and effective medium theory propagation regimes (Carcione, 2007).

2.1 Governing equations

We model isotropic viscoelastic SH-waves in the xz-plane ($\mathbf{x}=[x,z]^T$) using the Generalised Zener model. In this case, the polarization of the SH-wave is parallel to the y-axis. The equation of motion relates the $\sigma_{12}(\mathbf{x},t)$ and $\sigma_{23}(\mathbf{x},t)$ elements of the stress matrix to cross-plane displacement $u_2(\mathbf{x},t)$ is (Carcione, 2007):

$$\frac{\partial^2 u_2}{\partial t^2} = \rho^{-1}\left(\frac{\partial \sigma_{12}}{\partial x} + \frac{\partial \sigma_{23}}{\partial z} + f_2\right). \tag{1}$$

Here, $f_2(\mathbf{x},t)$ is the force per unit volume in the y-direction. The constitutive equations give the relation between stress and displacement,

$$\begin{aligned} \sigma_{23} &= \mu \frac{\partial u_2}{\partial z} + \mu \sum_{l=1}^{L_2} e_{23l}, \\ \sigma_{12} &= \mu \frac{\partial u_2}{\partial x} + \mu \sum_{l=1}^{L_4} e_{12l}. \end{aligned} \tag{2}$$

where $\mu(\mathbf{x})$ is the shear modulus. The summation in each equation allows to consider viscoelastic effects by introducing two relaxation functions, describing the anelastic properties along with the first and third component of motion. The finite-difference simulation of the constitutive equations uses memory variables ($e_{12l}(\mathbf{x},t)$ and $e_{23l}(\mathbf{x},t)$) in the stress-strain relationship, necessary to circumvent the convolution representing the deformation history of the material (Carcione & Cavallini, 1995).

We assume $L_2 = L_4 = 2$ and assign stress and strain relaxation times ($\tau_\sigma(\mathbf{x})$ and $\tau_e(\mathbf{x})$) dependent on two constant quality factors (τ_σ and τ_e - losses in the horizontal and vertical components) to each node. Following the Generalised Zener model:

$$\tau_\sigma = \frac{\tau_0}{Q_{H,W}}(\sqrt{Q_{H,W}^2+1}-1),$$
$$\tau_e = \frac{\tau_0}{Q_{H,W}}(\sqrt{Q_{H,W}^2+1}+1). \quad (3)$$

where τ_0 is the centre period. The memory variables satisfy the differential equation:

$$\frac{\partial e_{23l}}{\partial t} = (\frac{1}{\tau_\varepsilon}-\frac{1}{\tau_\sigma})\frac{\partial u_2}{\partial z} - \frac{\partial e_{23l}}{\partial \tau_\sigma},$$
$$\frac{\partial e_{12l}}{\partial t} = (\frac{1}{\tau_\varepsilon}-\frac{1}{\tau_\sigma})\frac{\partial u_2}{\partial x} - \frac{\partial e_{12l}}{\partial \tau_\sigma}. \quad (4)$$

Q_H and Q_W are quality factors at the centre frequency in the horizontal and vertical directions respectively, which were set first according to the General Fractional Zener Model, estimated for sandstone at a depth of 10 m (Liu & Greenhalgh, 2019). For nearly constant Q and if the sample has no internal interfaces, the two memory variables necessary to control viscoelasticity as well as the stiffness matrix parameters will be the same across the medium. This is the case at the start of the deformation process, where the sample is assumed as *isotropic* with no dissipation, and isotropic stiffnesses is deduced from Chen et al. (2007).

2.2 Perfectly matched layers

To suppress the reflecting waves from the sample boundary, we implemented the perfectly matched layers (PML) (Collino & Tsogka, 2001). PML is obtained by applying complex coordinate stretch to the wave equations (Chew & Weedon, 1994):

$$\tilde{x}_j = x_j + \frac{i}{\omega}\int_0^{x_j} \beta_j(m)dm. \quad (5)$$

where $\beta_j(x_j)$ is the variable dependent on the location, i is the imaginary unit and ω is the angular frequency. Outside PML, we have $\beta_j(x_j) = 0$. Inside PML, it is

$$\beta_j(x_j) = \beta_j(x_j(\bar{x}_j)) = \beta_0\left(\frac{\bar{x}_j}{l_p}\right)^2. \quad (6)$$

where $\bar{x}_j$ is the distance of the current location to the inner PML boundary line and $\beta_0 = \frac{-3c_{max}ln(R_c)}{2h}$. c_{max} is the maximum of the phase velocity of the media. R_c is the theoretical coefficient of PML (Komatitsch & Tromp, 2003) and h is the grid spacing. See **Figure 1** for an overview of the distribution of β_j.

The PML transforms $x_j \to \tilde{x}_j$. The spatial derivative becomes

$$\frac{\partial}{\partial x_j} \to \frac{\partial}{\partial \tilde{x}_j} = \frac{\partial}{\partial x_j}\frac{\partial x_j}{\partial \tilde{x}_j} = \frac{1}{s_j}\frac{\partial}{\partial x_j}. \tag{7}$$

where

$$s_j = 1 + \frac{i}{\omega}\beta_j. \tag{8}$$

The Fourier transform defines $\hat{g}(\omega) = \frac{1}{\sqrt{2\pi}}\int_{-\infty}^{\infty} \exp(-i\omega t)g(t)dt$. To implement the transform in frequency, we firstly apply Fourier transform to Equation (1) and set $f_2 = 0$,

$$(-i\omega^2)\hat{u}_2 = \rho^{-1}(\frac{\partial \sigma_{12}}{\partial \tilde{x}} + \frac{\partial \sigma_{23}}{\partial \tilde{z}}). \tag{9}$$

Substituting $\tilde{x}_j$ with s_j yields

$$(-i\omega^2)\hat{u}_2 = \rho^{-1}(\frac{\partial \sigma_{12}}{s_1\partial x} + \frac{\partial \sigma_{23}}{s_3\partial z}). \tag{10}$$

Multiplying $s_1 s_3$ to both sides of the equation leads to

$$s_1 s_3(-i\omega^2)\hat{u}_2 = \rho^{-1}(s_3\frac{\partial \sigma_{12}}{\partial x} + s_1\frac{\partial \sigma_{23}}{\partial z}). \tag{11}$$

Now we use Equation (8),

$$((\beta_1+\beta_3) - i\omega + \frac{i}{\omega}\beta_1\beta_3)\hat{u}_2 = \frac{1}{i\omega\rho}((1+\frac{i}{\omega}\beta_3)\frac{\partial \sigma_{12}}{\partial x} + (1+\frac{i}{\omega}\beta_1)\frac{\partial \sigma_{23}}{\partial z}). \tag{12}$$

Transforming the above equation back to the time domain, we can obtain the PML transformed equation of motion where we disregard the effect of source,

$$(\beta_1+\beta_3)\frac{\partial u_2}{\partial t} + \frac{\partial^2 u_2}{\partial t^2} + \beta_1\beta_3 u_2 = \frac{1}{\rho}(\frac{\partial \sigma_{12}}{\partial x} + \frac{\partial \sigma_{23}}{\partial z} + \beta_3\int dt\frac{\partial \sigma_{12}}{\partial x} + \beta_1\int dt\frac{\partial \sigma_{23}}{\partial z}). \tag{13}$$

With the similar procedure for Equation (2), the PML transformed constitutive relations are,

$$(\beta_1+\beta_3)\sigma_{23}+\frac{\partial\sigma_{23}}{\partial t}+\beta_1\beta_3\int dt\sigma_{23}=\mu\frac{\partial}{\partial t}\frac{\partial u_2}{\partial z}+\mu\beta_1\frac{\partial u_2}{\partial z}+\mu\frac{\partial}{\partial t}\sum_{l=1}^{L_2}e_{23l},$$
$$(\beta_1+\beta_3)\sigma_{12}+\frac{\partial\sigma_{12}}{\partial t}+\beta_1\beta_3\int dt\sigma_{12}=\mu\frac{\partial}{\partial t}\frac{\partial u_2}{\partial x}+\mu\beta_1\frac{\partial u_2}{\partial x}+\mu\frac{\partial}{\partial t}\sum_{l=1}^{L_2}e_{12l}. \quad (14)$$

It can be noted that the PML-transformed wave equations are identical to the original ones in the physical domain.

2.3 Implementation and optimisation method

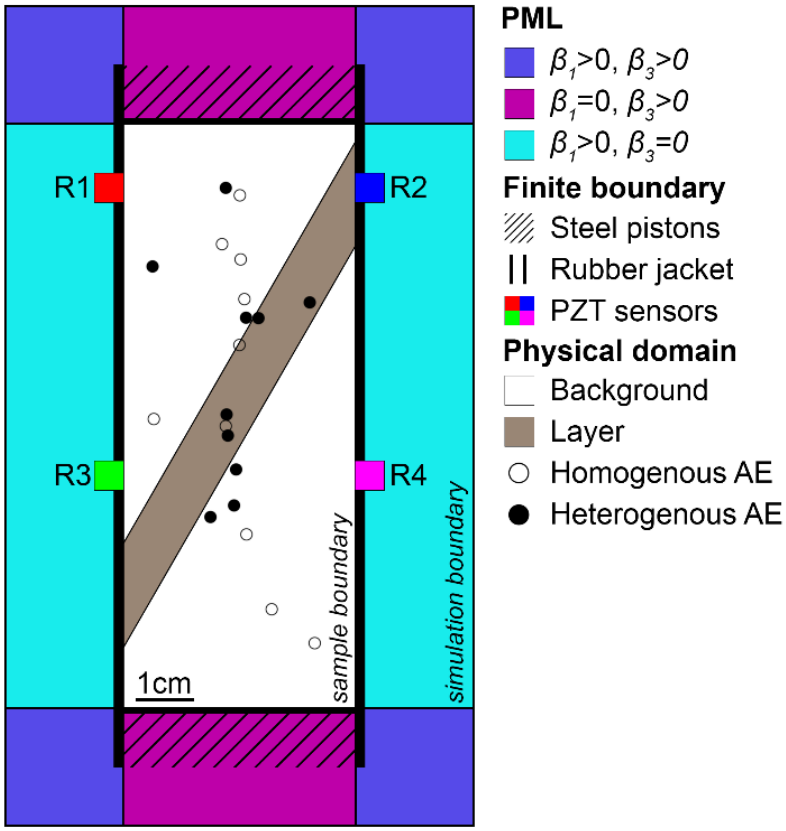

Figure 1: Implementation of the numerical model. Location parameters of the perfectly matching layers (PML) in axial (β_1) and radial (β_1) directions. Boundary conditions are constrained independently for steel piston and rubber jacket contacts. Acoustic emission (AE) arriving at piezo-electric transducers (PZT) located on the radial boundaries are modelled in the simulations for 1) a homogenous model and 2) a heterogeneous model with an inserted layer.

Genetic Algorithms (GA, Goldberg & Holland, 1988) are stochastic, population-based routines that optimise solutions through mutation and crossover amongst population members. They are suitable for constraining problems defined by relatively few parameters, assuming that a small but precise model space is preferable to a larger but poorly constrained one. With each generation, populations contain an increasing number of 'elite' solutions that fit the observed

data. We consider three primary elements that best represent the main features of the laboratory sample under deformation to parameterise the numerical model (**Figure 1**): (1) a homogenous isotropic background medium; (2) the finite boundary conditions of the sample edges (Yoshimitsu et al. 2016); (3) an inserted layer of decreased stiffness/Q that simulates the effect of a deforming zone of intense strain (Ji and Wang, 2011).

Viscoelastic parameters are modelled through variations in the SH-wave velocity (V_s) using the relationship $V_{SH} = \sqrt{k/\rho}$, where k refers to elements of the stiffness matrix (i.e., c_{44}, c_{66}). Densities (ρ) for the background medium and inserted layer are fixed as 2357 kg/m^3 and 1543 kg/m^3 (assuming an average density of 1950 kg/m^3 for a fractured medium, Kilburn, 2012; Yusuf et al., 2019). Velocity and attenuation are assumed to be isotropic for both the background medium and the inserted layer to homogenise the spatial behaviour. In analogy to the laboratory shear zone geometry, the inserted layer is set at a fixed angle of 60°, whilst its vertical offset (h) and thickness (l_a) is allowed to vary during the inversion. Boundary conditions are approximated through an infinitely thin layer along the sample edges. Separate conditions are assumed for the radial and axial boundaries to simulate the rubber jacket and steel piston contacts, respectively. The reflectivities of these surfaces are controlled through high variations in stiffness and density whose aim is to recreate the actual conditions of the sample contacts. Linear constraints of the inversion parameters are detailed in **Table 1**. The GA uses approximately 8 population members per invertible parameter (e.g., 10 parameters = 80 population members) and is run for a minimum of 8 generations with a mutation rate of 0.5. These parameters were selected through iterative testing of different model combinations.

Table 1: Linear constraints of SH-wave velocity (V_{SH}), Q, layer offset (h), layer thickness (l_a) and source location offset used in the genetic algorithm inversion.

Parameter	**Lower Bound**	**Upper Bound**
Background medium (V_{SH}, Q)	2000 m/s, 5	2500 m/s, 50
Boundary conditions (k, ρ)	2.5 GPa, 1 g/cc	30 GPa, 50 g/cc
Inserted layer (V_{SH}, Q)	1700 m/s, 5	2100 m/s, 20
Layer dimensions (h, l_a)	-10 mm, 0 mm	10 mm, 10 mm
Source location offset (x, z)	-5 mm, -5 mm	5 mm, 5 mm

Due to the inherent heterogeneity of the actual data, constraining the modelling parameters independently for all the experiment phases is impractical and computationally expensive. We apply the GA only to 40 waveforms (10 AE) selected (1) just before the start of the experiment

(Set 1) and (2) 40 waveforms selected shortly after sample failure (Set 2). P-wave arrival times for these events are manually picked. They have an estimated location error within 2 mm along the axis orthogonal to the failure plane (**Figure 1**). Set 1 assumes a homogenous isotropic starting model, while Set 2 assumes a heterogeneous isotropic starting model. The AE source is modelled as a ricker wavelet of duration 0.01 ms and a dominant frequency of 200 kHz, following the source characterisation of King et al. (2021).

Each AE event is forward modelled individually, and the wavefield is recorded at the sensors in **Figure 1**. As part of the inversion, source locations (*x, z*) are allowed to vary ±5 mm to account for errors in the observed data. In each case, modelled and observed arrivals are pre-filtered (bandpass sixth-order Butterworth) between 0.05 and 1 MHz to simulate the laboratory acquisition conditions and then filtered again between 175 and 225 kHz. The waveforms are normalised according to the second-highest amplitude arrival of the AE to minimise the effect of direction-dependent source amplitude variations (e.g., Kwiatek & Ben-Zion, 2013). Temporal weighting is applied to discretise the waveform as three dominant phases of:

1) Direct wave and near-source scattering arrivals from 0 to 0.06 ms;
2) Multiple reflections from the sample boundaries between 0.06 and 0.09 ms;
3) Late coda beyond 0.09 ms.

In addition, minor discrepancies in the precise timing of phase arrivals are compensated using dynamic time warping (Paliwal et al., 1982) within a window of 0.001 ms. The misfit for the GA is then calculated as the L2 normalisation between modelled and observed waveform data.

3 Results

3.1 AE wavefield

Shortly following source onset, multiple reflected waves propagate through the homogenous sample for AE Set 1 (**Figure 2a**; t=0.025ms). The result is a coda wavefield complicated by phase reversals and transmission losses at the sample boundaries at late lapse times. The reflections from the sample corners remain in phase. Despite the simplicity of the modelling, the simulated waveforms fit several phases and amplitudes for different source locations (e.g., **Figure 2b**, coloured waveforms). Velocity and Q values for the homogenous medium are solved as 2283 m/s and 18.5, respectively. At low frequencies and late lapse times, a vertically propagating wave (**Figure 2a**, axial reflections) dominates the wavefield, with high-amplitude arrivals in the modelled data from ~0.05 and ~0.14 ms (**Figure 2b**).

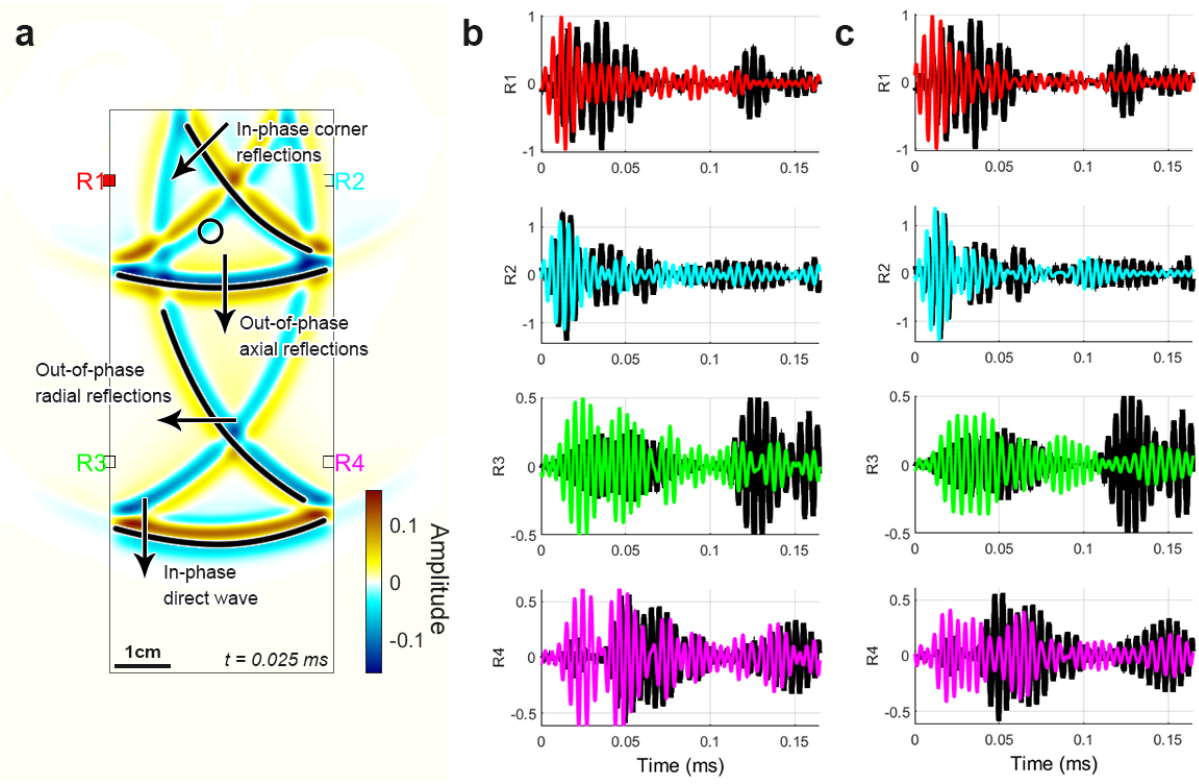

Figure 2: a) Wavefield for a single acoustic emission (AE, black circle) at time = 0.025 ms. Darker colours indicate higher amplitudes. b) Observed (black) and simulated (coloured) waveforms recorded at sensors R1-R4. c) There can be distinct variations in the relative timing and amplitude of different phase arrivals for the same AE depending on the location error.

Radial surface waves that would typically propagate along the boundary of the 3D sample (see Figure 6 of K22A) are not modelled by these 2D simulations, and their impact on the observed data remains uncertain. In simulations of AE propagating through cylindrical steel samples, Yoshimitsu et al. (2016) observed low-frequency surface waves arriving at 0.028 ms (max simulation length of 0.07 ms) for sources located on the surface of the sample. Due to the relative proximity of the AE source to the sample boundary, the mismatched amplitudes between 0.02 - 0.06 ms and at ~0.013 ms (**Figure 2b**) could be related to those arrivals. However, small offsets in the source location (<2 mm) resulted in distinct amplitude variations of different phase arrivals for the same AE (**Figure 2b,c**). Although the average location correction provided by the inversion was 1.6 mm, which is within the estimated 2 mm location error of the observed data, misfitting of off-axis reflections may also be playing a role in the simulations.

The GA solution could not stabilise to a single dominant solution for the heterogeneous medium when considering all the AE together, likely due to strong variability of near-source conditions. We thus simulated each event individually with the background medium and boundary condition properties constrained by the homogenous modelling. The Q within the

inserted layer was fixed at 12 by balancing the relative amplitudes between direct wave arrivals (0 – 0.06 ms) and axial reflections (0.06 – 0.09 ms). Source location offsets, layer thickness, and layer velocity were allowed to vary during the inversion. The GA is run for each AE for 8 generations with 80 population members. Solutions were collated, gridded, and then compared against the normalised inverse misfit (**Figure 3a**).

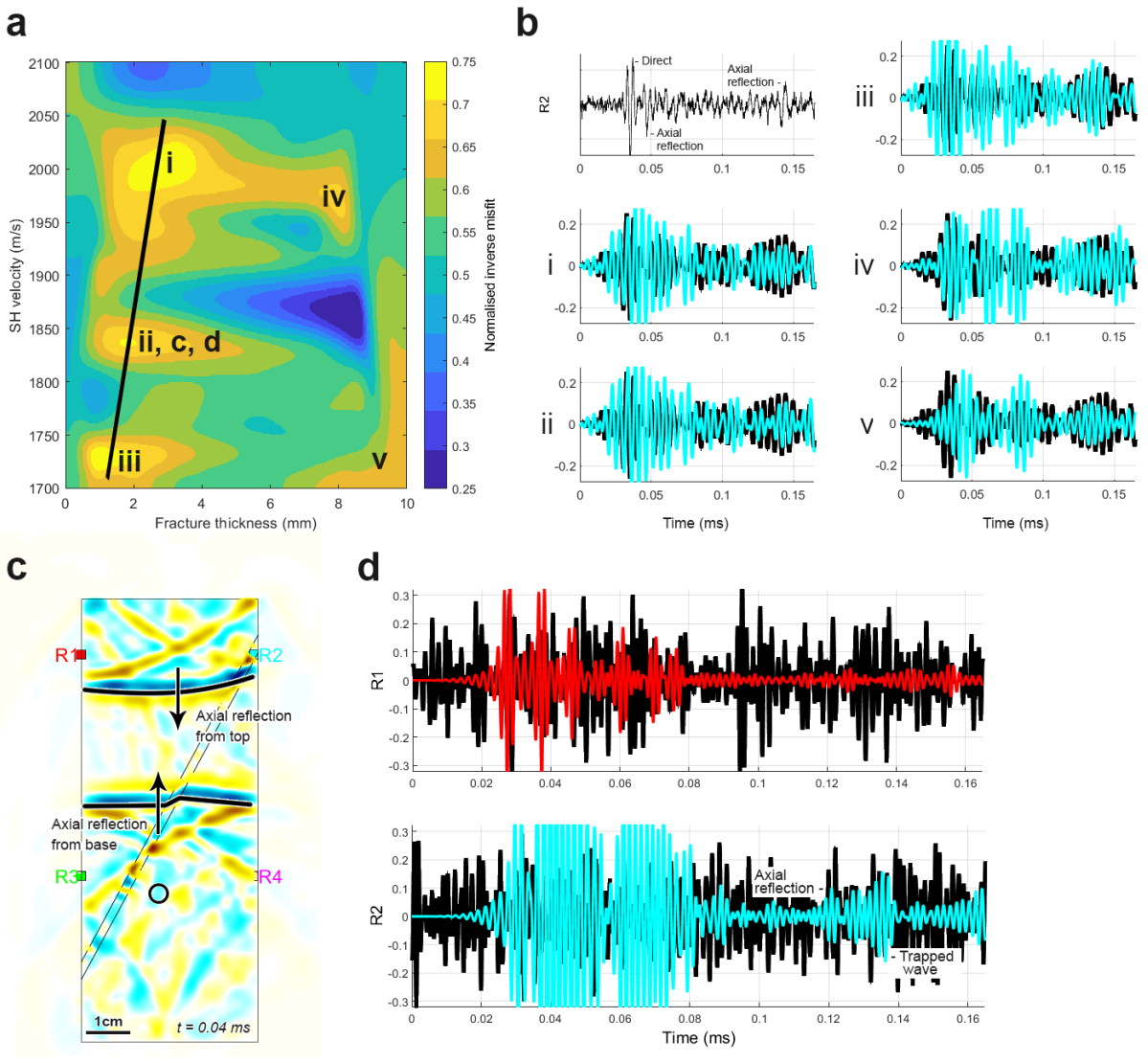

Figure 3: a) Dominant genetic algorithm solutions (i,ii,iii,iv,v) for fracture thickness and SH velocity. b) Simulation of a single acoustic emission (R2) for those values. c) Simulated wavefield at time = 0.04 ms for group ii. Axial reflections arrive at R2 at ~0.04 and 0.14 ms. d) High-frequency filtering (0.5 – 1 MHz) highlights a trapped-wave phase arrival at ~0.135 ms to R2 for group ii. This arrival is absent from R1.

The GA recognised five dominant groups having distinct properties that characterise the inserted layer (**Figure 3a,b i,ii,iii,iv,v**). Simulating each of the obtained conditions for a single AE reveals minor variations in waveform characteristics that could all fit the observed data (**Figure 3b**). Groups **i, ii,** and **iii** highlight a dominant fracture thickness of ~2 mm with velocities that range between 1725 and 2000 m/s. These properties fit the post-deformation

fault zone structure imaged and the physical properties measured in the laboratory (see Figure 1 of K22A). The PZTs used in the laboratory acquisition (see Table 1 of K22A) exhibit a high noise for the observed data at higher frequencies (**Figure 3d**, black waveforms). Therefore, it was impractical to use the GA beyond 500 kHz. Nonetheless, filtering simulated data to group **ii** highlighted a trapped-wave phase arrival to R2 at ~0.135 ms (**Figure 3d**, coloured waveforms). This arrival is notably absent from R1 suggesting that it occurs independently of the axial reflections and is related to interaction of the wavefield with the fault zone. Amplitude discrepancies between 0.05 and 0.09 ms for groups **iv** and **v** are due to insufficient attenuation of axial reflections that propagate through the layer (**Figure 3c**).

3.2 Synthetic modelling

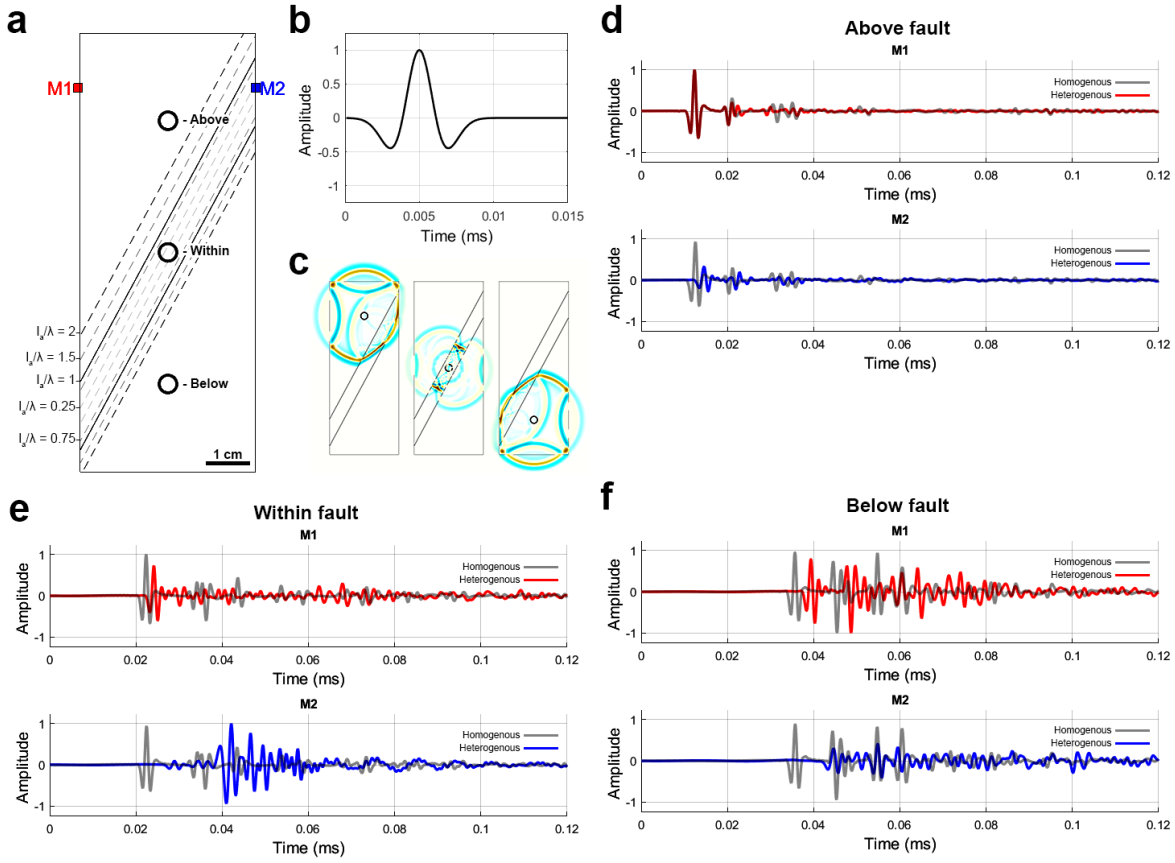

Figure 4: Synthetic modelling of acoustic emission (AE) sources. a) Sources are modelled with a fault zone of variable thickness between 0.25 and 2 wavelengths at 200 kHz. b) Source is modelled as a 200 kHz Ricker wavelet. c) At time = 0.015 ms, source energies strongly interact with the model boundary and inserted layer. Simulated waveforms for arrivals in homogenous (grey) and heterogeneous (coloured) models for sources located d) above, e) within, and f) below the fault zone.

In this analysis, three synthetic sources are modelled at off-fault (M1) and on-fault (M2) receivers: one above, one within and one below the fault zone (**Figure 4a-c**). To understand the relationship between the wavefield and fault zone structure (e.g. **Figure 4c**, t = 0.015 ms),

synthetic waveforms (filtered between 0.05 and 1 MHz, **Figure 4d-f**) demonstrate the effect of the inserted layer on phase arrivals. Boundary conditions, Q values, source properties (**Figure 4b**) and background velocity are fixed from the GA inversion. For all source positions in the homogenous model (**Figure 4d-f**, grey waveforms), waves recorded at M1 and M2 have a sharp direct arrival followed by discrete reflected arrivals from the sample boundaries. The relative source positions control the exact timing of these arrivals. With an inserted layer (**Figure 4d-f**, coloured waveforms), waveforms demonstrate a ~75% reduction in amplitudes for energy arriving at M2. Direct-wave arrivals to M1 mostly maintain their original amplitudes, with slight increases in arrival times. Reflected arrivals for the above-fault source (**Figure 4d**, coloured waveforms) show very little change in arrival times, highlighting weak interaction with the inserted layer at short hypocentral distances. At longer hypocentral distances (**Figure 4e-f**, coloured waveforms), strong scattering of the wavefield is observed for both M1 and M2. This is related to the strong interaction of the wavefield with the inserted layer, where constructive interference between acoustic boundaries can lead to late amplitudes that exceed the source content (e.g., **Figure 4e**, M2).

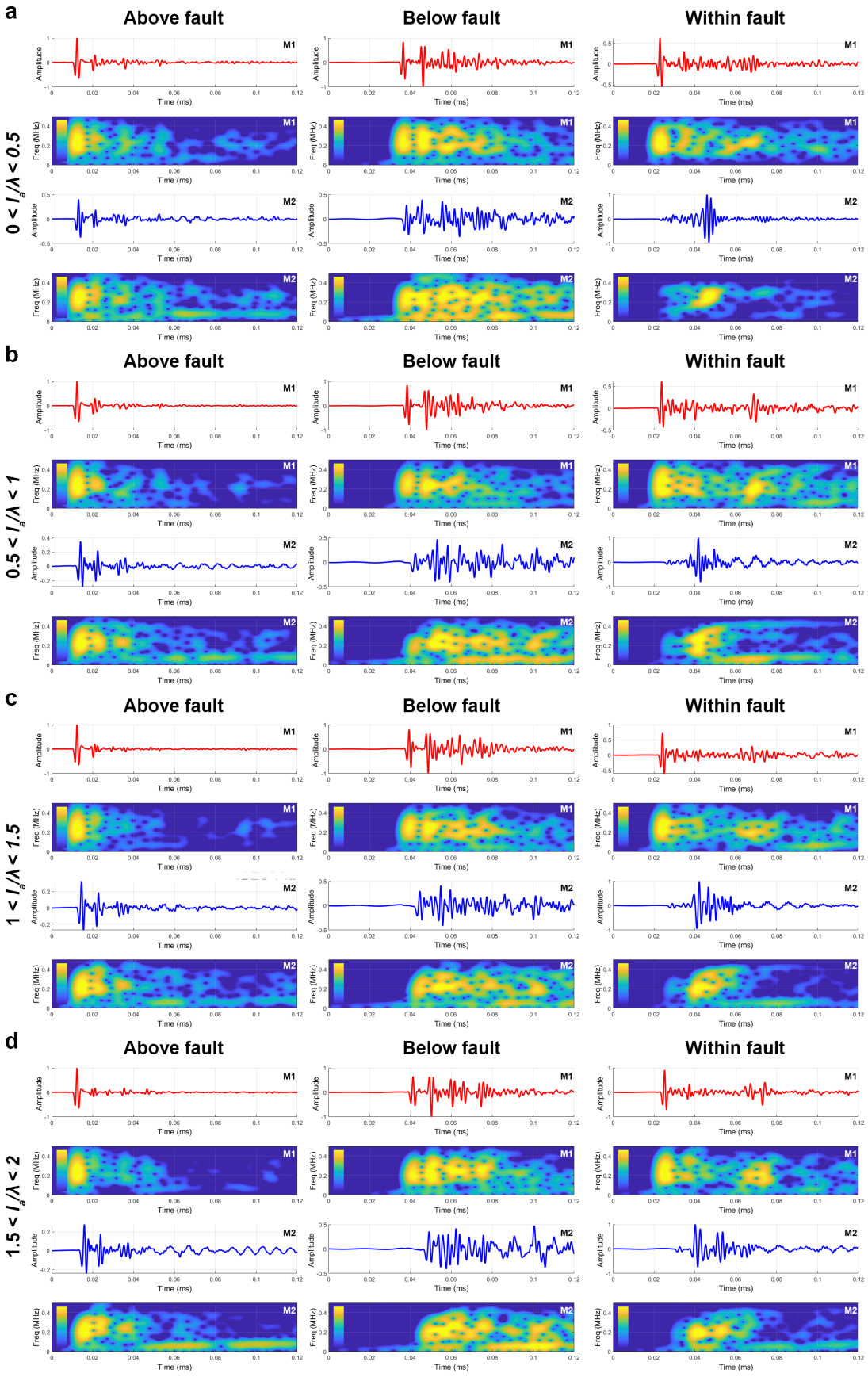

Figure 5: Waveforms and their short-term Fourier transform for energy propagating across a layer of increasing thickness. The ratio of thickness, l_a, to wavelength (λ = 8 mm at a velocity of 1600 m/s) spans a) l_a/λ <0.5, b) 0.5< l_a/λ <1, c) 1< l_a/λ <1.5 and d) 1.5< l_a/λ <2.

To investigate the wavelength-structure dependency of these arrivals, **Figure 5** displays waveforms and their short-term Fourier transform for energy propagating across a layer of increasing thickness as shown in **Figure 4a**. The ratio of thickness, l_a, to wavelength (λ = 8 mm at a velocity of 1600 m/s) spans from 0.25 to 2. Here we present the results for increasing ratios separated relative to the source fault geometry.

1. Above-fault AE (**Figure 5a-d**, left) – short earthquake-receivers distance:
    - With increasing ratios, waveforms at the off-fault receiver (M1) show direct-wave peaks of increasing amplitudes and decreasing energy in the low-frequency coda. The direct-wave peak always dominates the waveform.
    - To the contrary, waveforms at the on-fault receiver (M2) progressively lose high-frequency coda components, while their low-frequency coda intensifies. The amplitude ratio between direct and coda arrivals progressively decreases, increasing peak delays.
2. Below-fault AE (**Figure 5a-d**, centre) – long earthquake-receivers distance:
    - The effect of the fault zone is evident at both M1 and M2, with later arrivals dominating waveforms.
    - The direct wave packet is always distinct in both time and frequency spaces at M1 and it shows amplitudes consistent with those of the coda. Coda amplitudes are high-frequency and of short durations.
    - To the contrary, the separation between direct and later coda decreases at receiver M2. All recordings show a long energetic coda, particularly at low frequency.
3. Within-fault AE (Figure 5a-d, right) – near-source scattering and trapped waves:
    - Near-source scattering does not affect the direct-wave peak, which is dominant at M1; however, this improves localisation of a 200 kHz phase arrival at 0.06 ms. Low-frequency components and coda duration progressively increase.
    - However, neither M1 nor M2 show a low-frequency coda for this source at $0<l_a/\lambda<0.5$. The fault zone instead focuses the trapped wave between 0.04 and 0.05 ms. With increasing ratios, localisation decreases with the increase of later low-frequency coda.
    - The trapped wave peaks ~0.005 ms earlier (at 0.04 ms) when l_a/λ exceeds 1.5, with peak delays decreasing most drastically at $0.5< l_a/\lambda <1$, thus demonstrating that peak delays can decrease with increasing fault width.

4 Discussion

We have developed a model consisting of a layer of reduced stiffness/Q properties to characterise the development of damage within an isotropic homogeneous sample of Darley Dale Sandstone described in our companion paper (this volume, K22A). Models of scattering and absorption parameters for SH waveforms were obtained using experimentally-derived parameters and an inversion approach bounded within the limit of common variations of average values (**Table 1**, Heap et al., 2009; Kilburn, 2012; Yusuf et al., 2019). Although this simplifies the consequences of the coupling of fault-zone development with off-fault fracturing, our observations confirm inferences made from X-ray microtomography of crystalline samples (Renard et al., 2019). The results also support the use of peak delays, and more generally, the early coda, as reliable measurements of attenuation by scattering beyond the Markov approximation (Zhang et al. 2021; Napolitano et al. 2019), although with two important caveats:

1. The results obtained for within-fault source locations identify an anomalous decrease of peak delays with maximum amplitudes arriving ~0.03 ms earlier in the coda with increasing fault thickness (**Figure5b**, compare below-fault M2 and within-fault M1). The anomalous decrease represents the first evidence that higher heterogeneity does not necessarily mean higher scattering. A smaller fault zone causes constructive interference that focuses the trapped wave at a receiver in contact with the fault.
2. The proximity of the receiver location to the fault plays the primary role when considering delayed maximum amplitudes. This result goes beyond a standard description of site effects, as it demonstrates the sensitivity of near-fault observation to the entire fault structure, and particularly to fault width. Geology and geomorphology can dominate seismic recordings, as demonstrated by field-scale modelling using radiative transfer theory (Gabrielli et al. 2020). This is primarily the result of trapped and multiple-scattered waves dominating the envelope at receivers in contact with the highest heterogeneity (i.e., M2).

The results presented in this two-part study show that 3D rheological heterogeneities (e.g., Cionoiu et al., 2019) and sample boundary conditions (e.g., Yoshimitsu et al., 2016) likely hinder an accurate description of AE waveform data. However, neither of these features can be reproduced with 2D simulations to reduce uncertainties in the estimation of fault mechanics. We expect boundary conditions to be most relevant at frequencies where Rayleigh

scattering still dominates (<200 kHz). There, peak delays are most sensitive to surface wave arrivals for AE sources close to the sample boundary (see Figure 6 of K22A) and to axial reflections that quickly develop (**Figures 2, 3c**). As deformation progresses in heterogeneous samples and for receivers in contact with the fully developed fault zone, the signal created by surface waves strongly decreases (see Figure 5c of K22A). This leads to a dominance of boundary reflections that arrive shortly after source onset at ~0.04 ms and at ~0.014 ms (**Figure 3b**, R2). Our modelling thus suggests that the highest peak delays in the tomography are due to a combination of attenuation of the first set of arrivals and delay of the energetic second set, which interacts with the fault zone.

The primary reason to apply the modelling at 200 kHz is the noise sensitivity of the recording system at higher frequencies. It was impractical to use the GA at high frequencies (e.g., >500 kHz), where the shear zone was most evident. However, at an SH-wave velocity of 2283 m/s, scattering will move from quasi-homogeneous or Rayleigh at 150 kHz (ka=0.08) to resonant (Mie) at any frequency above it. At both frequencies there is the same scattering regime. The synthetic modelling highlights that a trapped wave develops inside any fully-developed layer within the Mie scattering regime (see l_a/λ>0.5 in **Figure 5b**). The results from the GA inversion indicated a dominant fracture thickness of ~2 mm with SH velocities that range between 1700 and 2050 m/s (**Figure 3a i-iii**). For l_a/λ=1, this corresponds to a frequency range of 0.5 – 1.15 MHz (**Figure 3d**), which correlates well with observations in the laboratory tomography (see Figure 6 of K22A).

Whilst the complexities induced by small-scale fluctuations are difficult to model, the inclusion of time-dependent heterogeneity across the sample affects the amplitude model and frequency variations across waveforms as a fault zone develops. Indeed, we observe propagation effects in the synthetic sample (where actual source-sensor distances are of the order of three to seven wavelengths) even if far-field approximations are not applicable. A wider variety of source, geometry, anisotropic and viscoelastic parameters than those demonstrated in this study is necessary to thoroughly model observations, especially coda waves. The inclusion of random fluctuations and the passage to a 3D description (Moczo et al., 2000) are required to test the reliability of the fits at different stages of fault development.

The upscaling of these results has significant implications on the ability of seismic arrays to observe variations of fracturing and strain in faults with absorption and scattering. Observations and models support the ability of peak delays and absorption parameters to assess spatial

changes of the Earth matrix in slow-deformation regimes, specifically fracture distribution and strain (Qiu et al., 2020). In this regime, high scattering and high absorption can identify the evolution of seismicity in active fault zones: from low stress areas characterised by developed fault zones identified at lower frequencies, to high stress regions of present seismic activity, visible at high frequencies (Napolitano et al., 2019).

Our results show that larger fault widths will unequivocally increase low-frequency late coda amplitudes (**Figure 5a-d**), a result that might have implications on the nucleation of long-period earthquakes without the need of fluids across faults, in settings alternative to low-cohesion volcanic sediments (Rowley et al. 2021). Depending on fault width, trapped waves can localise across a large portion of the coda, especially if the fault is not crossed in its entirety by direct-wave propagation (**Figure 5b-d**). This localisation leads to a drastic high-frequency reduction of coda duration. The results are differences in frequencies for scattering parameters that go well beyond the assumptions of radiative transfer theory. In controlled experiments, the combination of wave-equation modelling and peak delay imaging, whose physical description was grounded in radiative transfer modelling, could better discriminate the physics underlying the mapped structures. This combined approach, constrained by geological information appears to be a powerful tool to understand fault mechanics at the field scale.

5 Conclusions

Acoustic emission data from rock deformation laboratory experiments on Darley Dale Sandstone are modelled to relate scattering and coda parameters to the evolving fault structure. Using numerically-derived parameters bounded within a realistic range of measured observables, we demonstrate that modelling SH-waves propagating in a heterogeneous sample can quantify the role of important seismic and scattering attributes currently used at the field scale to map fault zones and understand their mechanics. The results depend on the relative geometry of sources, sensors, and areas of strain. They provide benchmarks on: (1) the ability of wave-propagation and effective medium theory to model seismic scattering and absorption parameters in rock deformation; 2) the onset of fault formation and the fracture growth, produced by the complex combination of on- and off-fault increase in microfracture volume; (3) the relevance of a simple peak delay or coda-attenuation analysis performed in tectonically active areas might have to measure fracturing, strain, and rheological changes affecting in- and off-fault volumes; (4) the potential of these parameters to detect the stage of deformation and the geometry and size of fracture networks within the system.

Our results show that scattering- and absorption-dependent mapping are valid markers of fracture networks and deformation-induced heterogeneities, if not a possible failure-forecasting attribute outside the small-scattering regime currently in use at the field scale. The consequences of extended trapped signals within coda envelopes, generally considered comprised uniquely of stochastic scattered waves, challenge our ability to apply simple analytical techniques to near-field imaging. Particular attention should be given to the frequency and heterogeneity scales assumed by stochastic-based imaging techniques, including seismic interferometry, where trapped waves could have an unexpected central role.

6 References

Aben, F. M., Brantut, N., Mitchell, T. M., & David, E. C. (2019). Rupture Energetics in Crustal Rock From Laboratory-Scale Seismic Tomography. *Geophysical Research Letters*, *46*(13), 7337–7344.

Benson, P. M., Thompson, B. D., Meredith, P. G., Vinciguerra, S., & Young, R. P. (2007). Imaging slow failure in triaxially deformed Etna basalt using 3D acoustic-emission location and X-ray computed tomography. *Geophysical Research Letters*, *34*(3). https://doi.org/10.1029/2006gl028721

Borleanu, F., De Siena, L., Thomas, C., Popa, M., & Radulian, M. (2017). Seismic scattering and absorption mapping from intermediate-depth earthquakes reveals complex tectonic interactions acting in the Vrancea region and surroundings (Romania). *Tectonophysics*, *706–707*, 129–142. https://doi.org/10.1016/j.tecto.2017.04.013

Calvet, M., Sylvander, M., Margerin, L., & Villaseñor, A. (2013). Spatial variations of seismic attenuation and heterogeneity in the Pyrenees: Coda Q and peak delay time analysis. *Tectonophysics*, *608*, 428–439. https://doi.org/10.1016/j.tecto.2013.08.045

Carcione, José M. (2007). *Wave fields in real media: Wave propagation in anisotropic, anelastic, porous and electromagnetic media*. Elsevier.

Carcione, Jose M., & Cavallini, F. (1995). The generalized SH-wave equation. *Geophysics*, *60*(2), 549–555.

Chen, Y., Wang, S., & Wang, E. (2007). Strength and elastic properties of sandstone under different testing conditions. *Journal of Central South University of Technology*, *14*(2), 210–215.

Chew, W. C., & Weedon, W. H. (1994). A 3D perfectly matched medium from modified Maxwell's equations with stretched coordinates. *Microwave and Optical Technology Letters*, *7*(13), 599–604.

Cionoiu, S., Moulas, E., & Tajčmanová, L. (2019). impact of interseismic deformation on phase transformations and rock properties in subductions zone. *Scientific Reports*, *9*(1), 1–6.

Collino, F., & Tsogka, C. (2001). Application of the perfectly matched absorbing layer model to the linear elastodynamic problem in anisotropic heterogeneous media. *Geophysics*, *66*(1), 294–307.

De Siena, L., Calvet, M., Watson, K. J., Jonkers, A. R. T., & Thomas, C. (2016). Seismic scattering and absorption mapping of debris flows, feeding paths, and tectonic units at Mount St. Helens volcano. *Earth and Planetary Science Letters*, *442*, 21–31. https://doi.org/10.1016/j.epsl.2016.02.026

De Siena, L., Amoruso, A., Pezzo, E. D., Wakeford, Z., Castellano, M., & Crescentini, L. (2017). Space-weighted seismic attenuation mapping of the aseismic source of Campi

Flegrei 1983–1984 unrest. *Geophysical Research Letters*, *44*(4), 1740–1748. https://doi.org/10.1002/2017GL072507

Di Martino, M. D. P., De Siena, L., Healy, D., & Vialle, S. (2021). Petro-mineralogical controls on coda attenuation in volcanic rock samples. *Geophysical Journal International*, *226*(3), 1858–1872.

Ekanem, A. M., Li, X. Y., Chapman, M., Ian, M., & Wei, J. (2014). Effect of Fracture Aperture on P-Wave Attenuation: A Seismic Physical Modelling Study. *ISRN Geophysics*, *2014*, 1–8. https://doi.org/10.1155/2014/241279

Frehner, M., & Schmalholz, S. M. (2010). Finite-element simulations of Stoneley guided-wave reflection and scattering at the tips of fluid-filled fractures. *Geophysics*, *75*(2), T23–T36.

Gabrielli, S., De Siena, L., Napolitano, F., & Del Pezzo, E. (2020). Understanding seismic path biases and magmatic activity at Mount St Helens volcano before its 2004 eruption. *Geophysical Journal International*, *222*(1), 169–188. https://doi.org/10.1093/gji/ggaa154

Goldberg, D. E., & Holland, J. H. (1988). Genetic Algorithms and Machine Learning. *Machine Learning*, *3*(2), 95–99. https://doi.org/10.1023/A:1022602019183

Heap, M. J., Baud, P., Meredith, P. G., Bell, A. F., & Main, I. G. (2009). Time-dependent brittle creep in Darley Dale sandstone. *Journal of Geophysical Research: Solid Earth*, *114*(B7).

Ji, S., & Wang, Q. (2011). Interfacial friction-induced pressure and implications for the formation and preservation of intergranular coesite in metamorphic rocks. *Journal of Structural Geology*, *33*(2), 107–113.

Kilburn, C. (2012). Precursory deformation and fracture before brittle rock failure and potential application to volcanic unrest. *Journal of Geophysical Research: Solid Earth*, *117*(B2). https://doi.org/10.1029/2011JB008703

King, T., Benson, P., De Siena, L., & Vinciguerra, S. (2020). Acoustic Emission Waveform Picking with Time Delay Neural Networks during Rock Deformation Laboratory Experiments. *Seismological Research Letters*. https://doi.org/10.1785/0220200188

King, T., Vinciguerra, S., Burgess, J., Benson, P., & Siena, L. D. (2021). Source Mechanisms of Laboratory Earthquakes During Fault Nucleation and Formation. *Journal of Geophysical Research: Solid Earth*, *126*(5), e2020JB021059. https://doi.org/10.1029/2020JB021059

Komatitsch, D., & Tromp, J. (2003). A perfectly matched layer absorbing boundary condition for the second-order seismic wave equation. *Geophysical Journal International*, *154*(1), 146–153.

Kwiatek, G., & Ben-Zion, Y. (2013). Assessment of P and S wave energy radiated from very small shear-tensile seismic events in a deep South African mine. *Journal of Geophysical Research: Solid Earth*, *118*(7), 3630–3641. https://doi.org/10.1002/jgrb.50274

Liu, X., & Greenhalgh, S. (2019). Fitting viscoelastic mechanical models to seismic attenuation and velocity dispersion observations and applications to full waveform modelling. *Geophysical Journal International*, *219*(3), 1741–1756.

Moczo, P., Kristek, J., & Halada, L. (2000). 3D fourth-order staggered-grid finite-difference schemes: Stability and grid dispersion. *Bulletin of the Seismological Society of America*, *90*(3), 587–603.

Napolitano, F., De Siena, L., Gervasi, A., Guerra, I., Scarpa, R., & La Rocca, M. (2019). Scattering and absorption imaging of a highly fractured fluid-filled seismogenetic volume in a region of slow deformation. *Geoscience Frontiers*. https://doi.org/10.1016/j.gsf.2019.09.014

Nishizawa, O., & Fukushima, Y. (2008). Laboratory experiments of seismic wave propagation in random heterogeneous media. *Advances in Geophysics*, *50*, 219–246.

Paliwal, K. K., Agarwal, A., & Sinha, S. S. (1982). A modification over Sakoe and Chiba's dynamic time warping algorithm for isolated word recognition. *Signal Processing*, *4*(4), 329–333. https://doi.org/10.1016/0165-1684(82)90009-3

Pyrak-Nolte, L. J., & Nolte, D. D. (1992). Frequency dependence of fracture stiffness. *Geophysical Research Letters*, *19*(3), 325–328. https://doi.org/10.1029/91gl03179

Pyrak-Nolte, L. J., Myer, L. R., & Cook, N. G. W. (1990). Transmission of seismic waves across single natural fractures. *Journal of Geophysical Research*, *95*(B6), 8617. https://doi.org/10.1029/jb095ib06p08617

Qiu, H., Allam, A. A., Lin, F.-C., & Ben-Zion, Y. (2020). Analysis of Fault Zone Resonance Modes Recorded by a Dense Seismic Array Across the San Jacinto Fault Zone at Blackburn Saddle. *Journal of Geophysical Research: Solid Earth*, *125*(10), e2020JB019756.

Renard, F., McBeck, J., Kandula, N., Cordonnier, B., Meakin, P., & Ben-Zion, Y. (2019). Volumetric and shear processes in crystalline rock approaching faulting. *Proceedings of the National Academy of Sciences*, *116*(33), 16234–16239.

Rowley, P., Benson, P. M., & Bean, C. J. (2021). Deformation-controlled long-period seismicity in low-cohesion volcanic sediments. *Nature Geoscience*, doi: 10.1038/s41561-021-00844-8.

Saito, T. (2002). Envelope broadening of spherically outgoing waves in three-dimensional random media having power law spectra. *Journal of Geophysical Research*, *107*(B5). https://doi.org/10.1029/2001jb000264

Sato, H., Fehler, M. C., & Maeda, T. (2012). *Seismic wave propagation and scattering in the heterogeneous earth*. Springer Science & Business Media.

Stanchits, S., Vinciguerra, S., & Dresen, G. (2006). Ultrasonic Velocities, Acoustic Emission Characteristics and Crack Damage of Basalt and Granite. *Pure and Applied Geophysics*, *163*(5), 975–994. https://doi.org/10.1007/s00024-006-0059-5

Takahashi, T., Sato, H., Nishimura, T., & Obara, K. (2007). Strong inhomogeneity beneath Quaternary volcanoes revealed from the peak delay analysis ofS-wave seismograms of microearthquakes in northeastern Japan. *Geophysical Journal International*, *168*(1), 90–99. https://doi.org/10.1111/j.1365-246x.2006.03197.x

Takahashi, T., Sato, H., Nishimura, T., & Obara, K. (2009). Tomographic inversion of the peak delay times to reveal random velocity fluctuations in the lithosphere: method and application to northeastern Japan. *Geophysical Journal International*, *178*(3), 1437–1455. https://doi.org/10.1111/j.1365-246x.2009.04227.x

Yoshimitsu, N., Furumura, T., & Maeda, T. (2016). Geometric effect on a laboratory-scale wavefield inferred from a three-dimensional numerical simulation. *Journal of Applied Geophysics*, *132*, 184–192.

Yusuf, B., Oloruntobi, O., & Butt, S. (2019). The formation bulk density prediction for intact and fractured siliciclastic rocks. *Geodesy and Geodynamics*, *10*(6), 446–454. https://doi.org/10.1016/j.geog.2019.05.005

Zhang, G., Li, H., Wang, M., Li, X., Wang, Z., & Deng, S. (2019). Crack-induced acoustic emission and anisotropy variation of brittle rocks containing natural fractures. *Journal of Geophysics and Engineering*, *16*(3), 599–610. https://doi.org/10.1093/jge/gxz031

Zhang, T., Sens-Schönfelder, C., & Margerin, L. (2021). Sensitivity kernels for static and dynamic tomography of scattering and absorbing media with elastic waves: a probabilistic approach. *Geophysical Journal International*, *225*(3), 1824–1853. https://doi.org/10.1093/gji/ggab048

582 Zhu, T., & Carcione, J. M. (2014). Theory and modelling of constant-Q P-and S-waves using
583 fractional spatial derivatives. *Geophysical Journal International*, *196*(3), 1787–1795.
584